Chapter II.5

Superconducting RF cavities

Fritz Caspers, Sergio Calatroni
CERN, Geneva, Switzerland

The application of superconducting materials in RF cavities has gained a huge interest in the particle accelerator field over the last five decades. In particular, the accelerating gradients have been increased considerably due to progress in the understanding of the limiting factors at the beginning. Such limiting factors were in particular multipacting and issues in surface preparation and related technology. Also, advances in material technology play a very important role. Today superconducting RF cavities are indispensable elements for many particle accelerators. A number of examples are presented and also measurement techniques for the characterisation of important RF properties.

1 Introduction and overview

As the very basics of superconducting RF (SRF) science were already discussed in Chapter II.4, this part will focus mainly on technological issues and applications. We start with an overview of the history of LEP where in the 80ies of the last century large-scale SRF cavity power plants were brought into operation at CERN. This extremely fruitful period has led to many technological improvements and has shown that superconducting cavity technology was mature enough for reliable operation. It also clearly demonstrated that running LEP at the required energy of about $100\,\mathrm{GeV}$ for electrons would have been practically impossible with normal conducting cavities. Note that for LEP, niobium-coated cavities were developed and employed. In parallel, outside the accelerator field, impressive progress was made in the field of SRF following the discovery of high-temperature superconductivity in 1986. Some examples include Josephson effect-based devices that permit building signal receivers and signal generators for very low (cryogenic) temperatures having quantum sensitivities and resolving even individual microwave photons. Other examples are superconducting Qubits, opening the door to quantum computer technology. For this lecture, we now turn from the very basics with a recap on skin depth and surface impedance both for normal conducting (NC) and superconducting (SC) cases to the RF properties of superconducting surfaces. The two-fluid model as a vital element for a proper understanding of SRF is mentioned, and examples of RF surface impedance are given and discussed.

Aspects of limits of validity of predictive theories for the RF surface impedance are also addressed. In a short section on general RF cavity theory, the equivalent circuit is presented and important quantities such as the loss factor R/Q , the transit time factor and the geometry factor G are introduced even though they were mentioned already in the previous lecture on "warm RF technology" (see Chapter II.2 on RF engineering). Their mutual dependencies from the shape of a superconducting cavity are discussed with

This chapter should be cited as: Superconducting RF cavities, F. Caspers and S. Calatroni, DOI: 10.23730/CYRSP-2024-003.1085, in: Proceedings of the Joint Universities Accelerator School (JUAS): Courses and exercises, E. Métral (ed.), CERN Yellow Reports: School Proceedings, CERN-2024-003, DOI: 10.23730/CYRSP-2024-003, p. 1085.

rather simple formulae and plots. In a following section, in which several selected methods for the measurement of RF surface impedance are introduced, an overview of this part of the technology is given, including its strengths and weaknesses. This also includes the way to measure the unloaded Q factor of a superconducting cavity which cannot be obtained via the classical vector network analyser transmission technique in the frequency domain but must be done in the time domain by measuring the time constant of the ringing of such kind of cavity. Related to the fabrication technology, many examples and different shapes also for low-energy beams are presented. In particular, finding the optimum shape of the longitudinal cut of this kind of cavities (elliptic cavities) has been a subject of research for decades. Radiation pressure-related mechanical vibrations (Lorentz forces) and their mitigation are another important parameter in SRF cavity structure design. Hot spots inside a SRF cavity, often caused by small pieces of dirt, and their location in operating conditions inside a test cryostat are a big challenge and the evolution of related test methods is presented together with an overview of the degrading effect. All this boils down to extreme requirements in production technology in terms of contamination and reliable production of clean and homogeneous surfaces. Finally, in the Appendix, several more theoretical aspects mentioned above are discussed in more detail as well as fundamental power and higher order mode couplers.

2 The history about RF superconductivity and LEP and the motivation for using SRF technology

The LEP machine at CERN is a nice example of transitioning from normal conducting RF accelerating cavities to superconducting technology. LEP was operating with electrons and positrons. Originally (LEP 1) this machine was optimized for $80\,\mathrm{GeV}$ using copper cavities. However, there was a strong demand from the physics community to increase the energy to above $100\,\mathrm{GeV}$. Using copper technology would have required 1280 cavities and $160\,\mathrm{MW}$ of RF power. If we are using copper cavities, one has to take into account that the RF power requirement is proportional to the 8^{th} power of the beam energy keeping in mind that $P \propto V^2$ and beam losses (synchrotron radiation losses) $\propto E^4$. For protons since E_0 is bigger by a factor of 1836 compared to electrons, the required RF power is much less critical and the bending radius is limited by the available bending fields for the same beam energy.

From Ref. [1] using the notation $U_0 =$ energy loss per particle over one turn, $\rho =$ machine radius, $E_\mathrm{b} =$ beam energy, $E_0 = 0.511\,\mathrm{MeV}$ for electrons and $938.245\,\mathrm{MeV}$ for protons, V_RF = total voltage from ALL cavities, $\phi_\mathrm{s} =$ synchrotron phase, lr_sh "longitudinal shunt impedance", and $I_\mathrm{tot} =$ total beam current, we can write the following equations

$$\mathrm{U}_0 \propto \frac{\mathrm{E}_\mathrm{b}^4}{\mathrm{E}_0^4}\frac{1}{\rho} = \mathrm{V}_\mathrm{RF}\sin\phi_\mathrm{s} \quad , \tag{II.5.1}$$

$$P_\mathrm{Cu} \propto \frac{V_\mathrm{RF}^2}{lr_\mathrm{sh}} \propto \frac{E_\mathrm{b}^8}{E_0^8}\,\frac{1}{\rho^2}\,\frac{1}{lr_\mathrm{sh}} \quad , \tag{II.5.2}$$

$$P_\mathrm{sc} \propto I_\mathrm{tot}\,U_0 \propto \frac{E_\mathrm{b}^4}{E_0^4}\,\frac{I_\mathrm{tot}}{\rho} \quad , \tag{II.5.3}$$

where P_Cu and P_sc are the power dissipated by normal conducting and superconducting cavities, re-

spectively. Obviously, using SC cavities is much more efficient with $P \propto E_{\mathrm{b}}^4$ (see II.5.3) vs. $P \propto E_{\mathrm{b}}^8$ (see II.5.2) in the NC case.

For protons (LHC) in a 27 km circumference ring, synchrotron radiation losses do not really have the same relevance since the E_0 of the proton is 1836 times higher compared to electrons. However, we have also for protons in LHC at 7 TeV certain synchrotron radiation losses.

At CERN's "open-air museum", one can still see an energy storage device (a nearly one-meter diameter sphere on top of a big copper tube as an accelerating structure, see Fig. II.5.1) which was developed in the early 80$^{\mathrm{ies}}$ (before the SRF time in LEP) with the aim to bring the high field-strength only on that time window to the NC accelerating cavity when one of the few electron bunches (evenly distributed over the 27 km circumference) is passing by.

Fig. II.5.1: Normal conducting CERN LEP cavity with a spherically-shaped storage cavity on top [2].

The reason for using SC cavities is thus very simple: to obtain very high accelerating fields in continuous mode, the power dissipated by normal conducting (i.e. copper) cavities becomes too large. In addition, we should keep in mind that for NC cavities there is a relatively high R/Q together with a moderate Q while SC cavities allow designs with larger beam pipes that have a lower R/Q with high Q which is more favorable for beam stability (loss factor). In other words, SC can provide high voltage at low R/Q. This permits a reduction of the machine radius R_{a} since higher synchrotron radiation can be supported as SC cavities provide more longitudinal kick compared to NC cavities. This would be unacceptable for NC cavities, but owing to the huge Q_0 the performance of SC cavities does not suffer much. Remember that there can be a 10^5 difference in the surface resistance R_{s}, thus in dissipated power, for the same surface fields.

This is also valid taking into account the efficiency of the cryogenic plant. The Carnot efficiency of a perfect cooler working between 300 K and T is given in Eq. (II.5.4) with T in Kelvin

$$\eta_{\mathrm{c}} = 300 - \frac{\mathrm{T}}{300 - \mathrm{T}} \quad . \tag{II.5.4}$$

For $\mathrm{T} = 4.2\,\mathrm{K}$, we obtain the theoretical $\eta_\mathrm{c} = 0.014$. A modern cryo plant has a technical efficiency that can reach about 30% of the ideal one, thus $\eta_\mathrm{real} = 0.0042$. Even taking this into account the energy savings are huge.

Copper cavities already get really hot with one $\mathrm{MV/m}$ surface field. Good SC cavities can do $30\,\mathrm{MV/m}$ and in contrast to NC cavities, there is very little power loss between subsequent bunches and reasonably strong coupling to the generator provided. The normalisation "per meter" refers here to the length of the cavity sections, thus the internal field inside the cavities is locally somewhat higher than the numbers shown here. In the LEP case we had:

- Cu hypothesis : $3\,\mathrm{MW/m}$ at $3\,\mathrm{MV/m}$ accelerating field;
- SC case: $3\,\mathrm{W/m}$ at $5\,\mathrm{MV/m}$ accelerating field returning $3\,\mathrm{kW/m}$ including cryogenic losses.

For LEP2 we have to remember that 48 copper cavities gave an absolute maximum accelerating voltage of $150\,\mathrm{MV}$ however in practical operation more realistically rather $120\,\mathrm{MV}$. Now on the other hand, 72 superconducting modules (each with four cavities) returned $2910\,\mathrm{MV}$ (design maximum), and applying a correction factor of 0.96 one gets $2790\,\mathrm{MV}$ and assuming that two units would trip we arrive at $2630\,\mathrm{MV}$. Pushing the gradient to $6.5\,\mathrm{MV/m}$ we got an electron energy of $98\,\mathrm{GeV}$, pushing further to $7\,\mathrm{MeV}$ ($3200\,\mathrm{MV}$ accelerating gradient) we obtained $100\,\mathrm{GeV}$. However, it was decided to stay for operational reasons at $6.8\,\mathrm{MeV}$ ($3120\,\mathrm{MV} + 180\,\mathrm{MV}$ unit in reserve). Regarding quantum lifetime see e.g. Ref. [3]. For a good quantum lifetime (related to synchrotron radiation) a sufficient RF bucket height is required.

All this was a technically highly challenging approach to exploring new technological territory and standing under high pressure. Lots of hardware was burnt. And now quoting a word of Steve Myers when $102\,\mathrm{GeV}$ was reached on the question: "How did we get there?" Answer: "By lowering the luminosity and breaking cavities", and "can we go further?" "Yes by lowering further the luminosity and breaking more cavities" (see Fig. II.5.2).

Fig. II.5.2: The RF groups' 1999 collection of burnt RF items in LEP [4].

Now coming to the abridged story of the Year 2000: On 14 June 2000, a first candidate event (ALEPH) was found at $206.7\,\mathrm{GeV}$ with a reconstructed Higgs mass of $114.3\,\mathrm{GeV}/c^2$. All this was not far from getting the Higgs at that time already in LEP. Finally, in September 2000 one more month of

extension of this run was granted before finally shutting LEP down, in order not to delay further the LHC. A very good overview on SC cavity development at CERN until 2000 can be found in Ref. [5].

Now we are moving away from CERN and in particular LEP-related historical stories on superconducting cavities and just give a brief overview of what else has gone on in the field of microwave superconductivity.

A good and recent (Jan 2021) discussion on the evolution of SRF science and technology (not only related to particle accelerator applications) was given in an excellent paper by Steven M. Anlage (see Fig. II.5.3) [6]. That paper also gives a nice overview of the theory and related physical phenomena in the superconducting regime. Highlights include the discovery of high-temperature superconductors in 1986 and cryogenic microwave photon detectors, as well as single microwave photon sources.

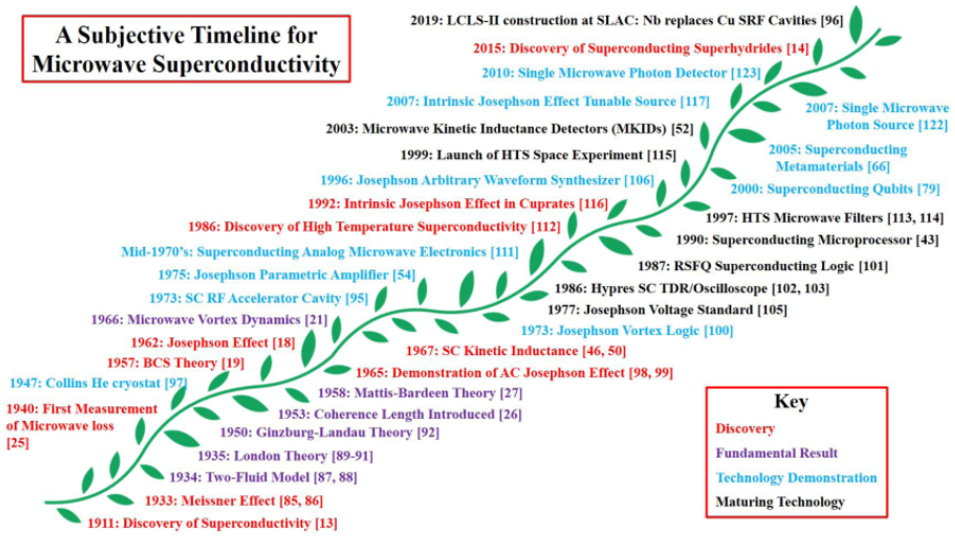

Fig. II.5.3: Overview of microwave superconductivity evolution [6].

SRF is a hot and interesting field, despite cryogenic technology. We could spend a lot of time just on this subject alone, discussing all the inventions and new effects there in detail, but we will close here.

After this historical overview and introduction, we now can go "medias in res". Let us start with a short recap of the visualisation of the "resistance per unit square".

3 A short recap on the SRF theory

Since we will deal a lot with the surface resistance R_s, here is a simple DC model that gives a rough idea of what it means (see Fig. II.5.4). Consider a square sheet of metal of thickness d and of length of each side a, of specific resistivity $\rho = [\Omega\,\mathrm{m}]$ and calculate its resistance to a (DC) transverse current flow. We call this $R_\square$ (read: "resistance per unit square")

$$R_\square = \frac{\rho\,\mathrm{a}}{\mathrm{d}\,\mathrm{a}} = \frac{\rho}{\mathrm{d}} \quad . \tag{II.5.5}$$

The surface resistance R_s is the resistance that a square piece of conductor opposes to the flow of

the currents induced by the RF wave, within a layer δ (skin depth). The equation is very similar to that of $R_\square$, with the thickness d replaced by the skin depth δ

$$R_s = \sqrt{\frac{\mu_0 \omega}{2\sigma}} = \frac{1}{\sigma\delta} = \frac{\rho}{\delta} \quad , \tag{II.5.6}$$

where $\delta = 1/\sqrt{\pi f \mu_0 \sigma}$, f is the frequency of the Rf wave and $\sigma = 1/\rho$ is the electrical conductivity.

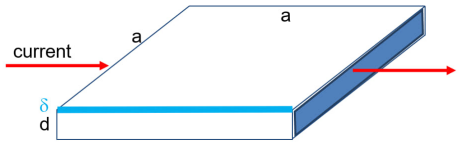

Fig. II.5.4: Visualisation of the resistance per unit square.

For DC we talk about $R_\square$ (read: "resistance per unit square") as there is ∞ skin depth or $\delta = \infty$. As an example, you may consider using a metal plate of say $100 \times 100\,\mathrm{mm}$ with $10\,\mathrm{mm}$ thickness and assuming perfectly conducting electrodes (in red) on the opposite sides. Thus, a homogenous current flow through the device under test (DUT) i.e. the metal or maybe also a carbon plate is assured.

- **Quiz**: Why is $R_\square$ (for DC) and R_s (for RF) dimension less?

- **Question**: Use some values for a and calculate $R_\square$ for e.g. $a = 1\,\mathrm{mm}$ and also $a = 1\,\mathrm{m}$, assume copper with a specific resistance $\rho = 17\,\mathrm{m\Omega[mm^2/m]}$. Of course, one can also write in as $1.7 \times 10^{-8}\,\Omega\,\mathrm{m}$.

In contrast, take note of the skin depth (for RF) thickness δ of the blue layer; for $1\,\mathrm{MHz}$ and copper δ amounts to $64\,\mu\mathrm{m}$ and about $2\,\mu\mathrm{m}$ for $1\,\mathrm{GHz}$. This notation $[\mathrm{mm^2/m}]$ to write the unit of resistivity, visualizes a copper wire with $1\,\mathrm{mm}$ cross-section and $1\,\mathrm{m}$ length ($= 17\,\mathrm{m\Omega\,m}$).

For a proper understanding of the surface impedance concept, a short recap of this concept can be useful. Let us assume a homogeneous plane wave (arriving from vacuum into z-direction) with normal incidence and vertical polarisation (see Fig. II.5.5). Obviously, E and H are pointing in the x direction and y direction respectively, and are mutually orthogonal. Thus the complex surface impedance Z_s can be defined as

$$\mathrm{Z}_s = R_S + jX_S = \frac{E_\parallel(0)}{H_\parallel(0)} \quad , \tag{II.5.7}$$

where $z = 0$ is on the surface.

We take Maxwell's equation, set the appropriate boundary conditions for the continuity of the waves (incident, reflected, transmitted), and we get

$$Z_S = \frac{E_\parallel(0)}{H_\parallel(0)} = \sqrt{\frac{j\omega\mu_0}{\sigma}} = \sqrt{\frac{\omega\mu_0}{2\sigma}} + j\sqrt{\frac{\omega\mu_0}{2\sigma}} = R_S + jX_S \quad , \tag{II.5.8}$$

and compare this with II.5.6 above.

Please note that the real part and imaginary part of the surface impedance for metals are equal

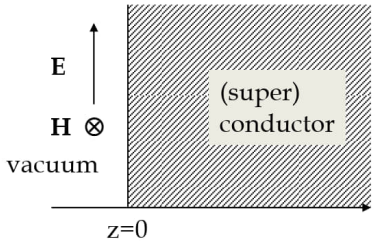

Fig. II.5.5: Homogeneous plane wave with normal incidence to a half-space.

(i.e. phase = 45 deg) only for the ideal case; with surface roughness the real part increases but in particular and much stronger the imaginary part for high frequencies [7].

- **Question**: Introducing appropriate numbers, e.g. for copper at ambient temperature $\sigma_{\mathrm{Cu}} = 58.5 \times 10^6 \mathrm{S/m}$ where $\mathrm{S/m}$ stands for "Siemens per meter" and calculate R_s for $f = 1\,\mathrm{GHz}$.
Answer: $R_s = 8.2\,\mathrm{m\Omega}$.

- **Question**: What is the skin depth δ at $1\,\mathrm{GHz}$ for copper?
Answer: About $2\,\mu\mathrm{m}$.

- **Short quiz**: What is the skin depth in copper at ambient temperature for $50\,\mathrm{Hz}$ and also for $1\,\mathrm{MHz}$?
Hint: use scaling!

- **Short quiz**: How about stainless nonmagnetic steel with a 50 times lower conductivity than copper?

- **Question**: What happens for magnetic steel?
Hint: the formula for skin depth is replaced by $\delta = 1/\sqrt{\pi f \mu_0 \mu_r \sigma}$.

3.1 The two-fluid model

Now, we will discuss the two-fluid model and cooper pair inertia (see Chapter II.4 on superconductivity). In dynamic mode (AC, pulsed, RF):

- Cooper pairs have some inertia thus the RF H field is not fully screened;
- Normal electrons also "feel" the field;
- Current is carried by both types of charge carriers (NC and SC);
- The process is dissipative.

All free electrons (from the conduction band) of density n of the superconductor are divided into two groups:

- superconducting electrons of density n_s,
- normal electrons of density n_n,

with $(n_s + n_n)/n = 1$.

As the temperature increases from 0 K to the critical temperature T_c, the density n_s/n decreases from 1 (all e^- in the form of Cooper pairs) to 0 (all Cooper pairs broken) when the material becomes normal conducting. If the current is constant (at $n_s/n = 1$), the electric field E cannot appear inside the superconductor because otherwise the superelectrons would be continuously accelerated and the current would increase infinitely. These two branches of normal electrons and superelectrons are illustrated in Fig. II.5.7. If there is no electric field, the normal electrons are at rest: only the super electrons carry the current in a steady state, and they do not scatter on the impurities thanks to a coherent state (see below). The first London equation shows that the electric field differs from zero only when the current density varies over time. It describes the ballistic flow of super-electrons in place of Ohm's law (which describes the viscous flow of electrons in a metal) and gives J_s as a function of the vector potential A.

This gives rise to the surface resistance as predicted by the Bardeen–Cooper–Schrieffer theory (BCS), R_{BCS}.

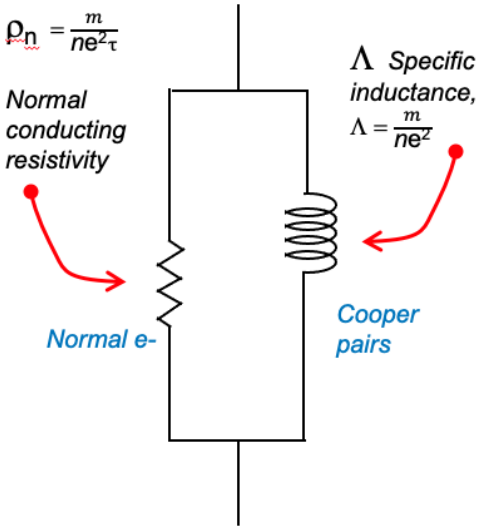

Fig. II.5.6: Equivalent circuit for a superconductor (see Chapter II.4 on superconductivity).

3.2 The BCS surface resistance

The BCS surface resistance can be calculated by

$$R_{\mathrm{BCS}} = A\left(\lambda_L^4, \xi_F, \ell\right)\frac{\omega^2}{T}e^{-\Delta/k_BT} \quad , \tag{II.5.9}$$

where Δ is the superconducting energy gap (binding energy of Cooper pairs), k_B is the Boltzmann constant, ω is the angular frequency, T the temperature and A a proportionality constant that depends on the London penetration depth λ, on the dimension of the Cooper pairs ξ_F and on the electron mean free path ℓ (i.e on the normal state conductivity σ_n).

More explicitly (but still approximate):

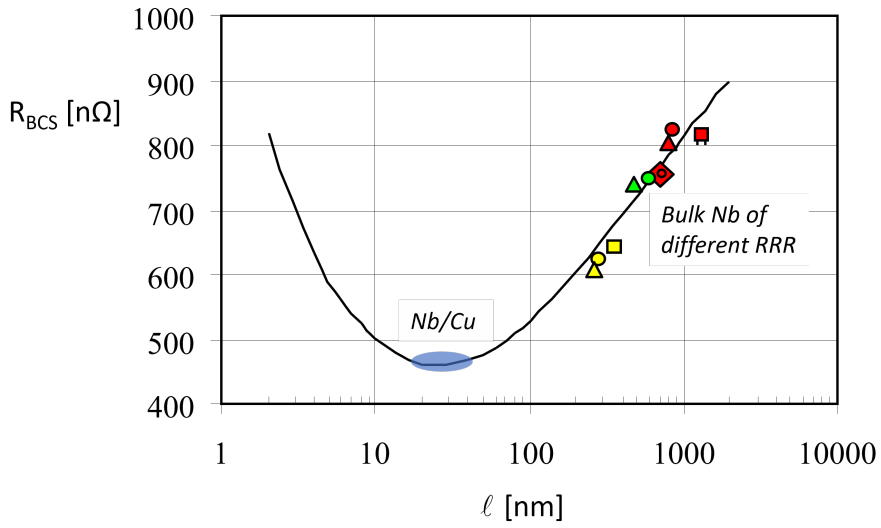

Fig. II.5.7: Niobium surface resistance as a function of electron mean free path ℓ at 1.3 GHz (see Chapter II.4 on superconductivity).

$$R_s^{\mathrm{BCS}}(\omega,T) = \mu_0^2\omega^2\sigma_{n0}\lambda^3\frac{\Delta}{k_B}\ln\left(\frac{\Delta}{\hbar\omega}\right)\frac{e^{-\Delta/k_BT}}{T} \approx R_s^{\mathrm{BCS}}(\omega,T) = \frac{A}{T}\omega^2\exp\left(-\frac{\Delta}{k_BT}\right) \quad , \tag{II.5.10}$$

$$R_s^{\mathrm{BCS}} = 1.3\times10^{-10}\,[\Omega]\times(f\,[\mathrm{MHz}])^2\times\frac{1}{T}\times\exp\left(-\frac{17.67\,[\mathrm{K}]}{T\,[\mathrm{K}]}\right) \quad . \tag{II.5.11}$$

The material parameter dependence of $R_s^{\mathrm{BCS}}(T,f)$ is discussed extensively in [8]. For example, R_{BCS} has a minimum at RRR (Residual Resistivity Ratio, i.e. the resistivity at room temperature divided by the resistivity at low temperature, and indicator for metal purity) of 20 for niobium, i.e. when electron mean free path ℓ is equal to the superconducting coherence length (the size of Cooper pairs) ξ_F, see Fig. II.5.7.

The actual RF surface resistance is

$$R_s = R_s^{\mathrm{BCS}} + R_{\mathrm{res}} \quad , \tag{II.5.12}$$

where R_s^{BCS} can be calculated theoretically as discussed above from material parameters (resistivity, critical temperature, etc.) and depends on temperature. This is well illustrated in Fig. II.5.9. The residual resistance R_{res} usually depends on "unpredicted" extrinsic phenomena or exotic properties of the material as discussed later, such as defects, normal-conducting inclusions, surface contamination, crystalline state, and flux trapping. At first order, it does not depend on temperature. R_{res} cannot be predicted from (im)purity (RRR).

Let's make a numerical example for comparison with the results from the graphic in Fig. II.5.8.

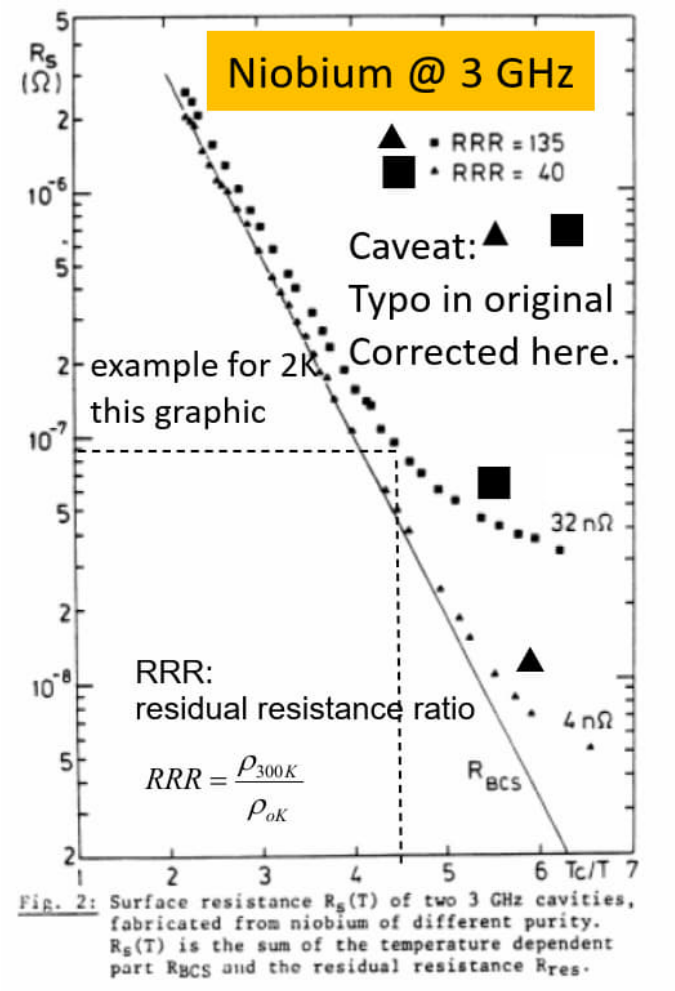

Fig. II.5.8: Comparison of surface resistance for two values of RRR [9].

For $f = 3\,\mathrm{GHz}$ ($\omega = 2\pi f$ and $T = 2\,\mathrm{K}$). Agreement is quite good for the $32\,\mathrm{n\Omega}$ trace since this formula is good for not too pure materials (rather low RRR values)

$$R_s\,[\mathrm{ohm}] = 1.3 \cdot 10^{-10}\,(3000)^2 \cdot 1/2 \cdot e^{(-8.83)} = 8.7 \cdot 10^{-8}\,[\mathrm{ohm}] \quad . \tag{II.5.13}$$

3.3 RF residual resistance or the limits of predictive theories

- RRRs (sometimes quoted R_0): Not predicted by BCS!
- Contains the (initially) "unknown".
- Existence of pinning center (e.g. remnant of damage layer, thermal strain, poor recrystallization).
- Flux trapped during cooldown
  - Mitigation: Magnetic hygiene (non-magnetic steel for nuts and bolts. Active and passive magnetic shielding of the cryostat. Cool-down procedures. $\rightarrow Q_0 \times 10$ improvement!

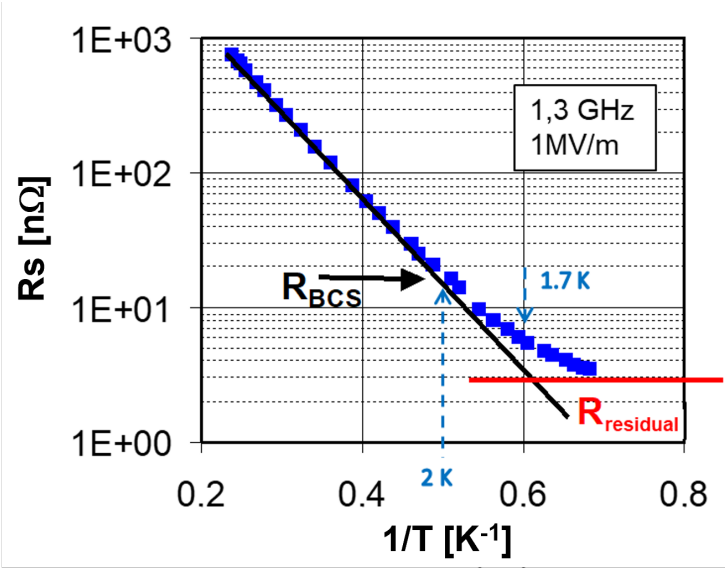

Fig. II.5.9: R_{BCS} vs. temperature for bulk Nb at 1.3 GHz (see Chapter II.4 on superconductivity).

- Other pair breaking mechanism:
  - Existence of magnetic impurity (e.g. vacancies in the oxide layer),
  - Proximity effect (there is a metallic layer at the metal oxide interface: $NbO \Rightarrow SC$ by proximity effect but affects the gap).
- Other suspects (not yet identified).

Questions:

- What is the ratio in surface impedance around 1 GHz between copper at ambient temperature and niobium at 2 K (A = nearly equal; $B = 10^5$; $C = 10^{-3}$)?
- Cooling a superconductor down to a few K requires a cryo plant; what is the ratio for one Watt dissipated at cryogenic level (4.2 K; LEP case) and the related compressor power on the surface? ($A = 3$, $B = 10$, $C \approx 250$)
- There was a hypothetical scenario for LEP using copper cavities with $5\,\mathrm{MV/m}$ accelerating field; the required power would have been: $A = 100\,\mathrm{kW/m}$, $B = 10\,\mathrm{kW/m}$, $C = 3\,\mathrm{MW/m}$.
- For LEP the SC cavity scenario (Nb case) for $5\,\mathrm{MV/m}$ accelerating field returned cavity losses at the cryo level of: $A = 1\,\mathrm{kW/m}$, $B = 30\,\mathrm{W/m}$, $C = 7\,\mathrm{kW/m}$.
- For LEP the total loss including cryo plant and $5\,\mathrm{MV/m}$ were: $A = 7\,\mathrm{kW/m}$, $B = 1\,\mathrm{MW/m}$, $C = 50\,\mathrm{W/m}$.
- What is the technical efficiency of a modern cryo-plant compared to the theoretical value (Carnot efficiency): $A = 3\%$, $B = 90\%$, $C = 30\%$.
- In an electron machine like LEP, the RF power required to compensate synchrotron radiation losses ($2\,\mathrm{kW/m}$) scales with particle energy E (momentum) as: $A \propto E^2$, $B \propto E^4$, $C \propto E^8$.
- Comparing copper and SC cavities the power requirements vs. accelerating voltage would scale as

A: $P_{cu} \propto E^8$ and $P_{sc} \propto E^4$, B: $P_{cu} \propto E^4$ and $P_{sc} \propto E^8$, C: $P_{cu} \propto E^6$ and $P_{sc} \propto E^3$.

4 A short recap on RF cavity theory

4.1 Equivalent circuits

The well-known equivalent circuit for an RF cavity coupled to a generator and to the particle beam is illustrated in Fig. II.5.10 has already been discussed in detail in the conventional RF course, thus here is only mentioned as a recap. We meet the resonant condition when

$$\omega L = \frac{1}{\omega C} \quad . \tag{II.5.14}$$

The resonant frequency f_{res} (angular frequency ω_{res}) is given by

$$\begin{aligned} \omega_{\text{res}} = 2\pi f_{\text{res}} = \frac{1}{\sqrt{LC}} \Rightarrow \\ \Rightarrow f_{\text{res}} = \frac{1}{2\pi}\frac{1}{\sqrt{LC}} \quad . \end{aligned} \tag{II.5.15}$$

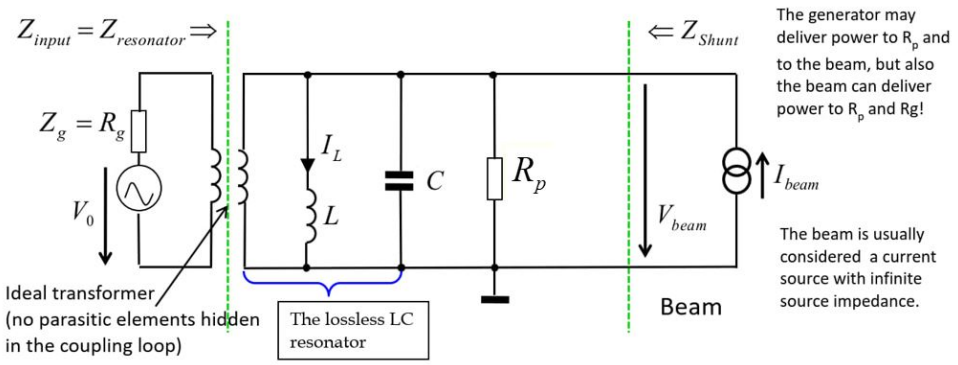

Fig. II.5.10: Equivalent circuit for a cavity coupled to a generator and to the beam [10].

4.2 Resonators

An accelerating RF cavity is indeed a resonator for an electromagnetic wave. We already mentioned the idea of comparing an RF cavity to an RLC circuit. Two important quantities characterize a resonator (remember your first physics course): the resonance frequency f_0 and the quality factor Q_0

$$Q_0 = \frac{f_0}{\Delta f} = \frac{\omega_0 W}{P_c} \quad , \tag{II.5.16}$$

where P_c/ω_0 is the wall current losses per RF period and W is the stored energy in the cavity volume. As for any resonator, the (field) amplitude when the power source is turned off follows the equation $E(t) = E_0 \exp(-t/\tau_0)$ and τ_0 is the time constant for unloaded Q_0, $\tau_0 = Q_0/\pi f_0$, see Fig. II.5.11.

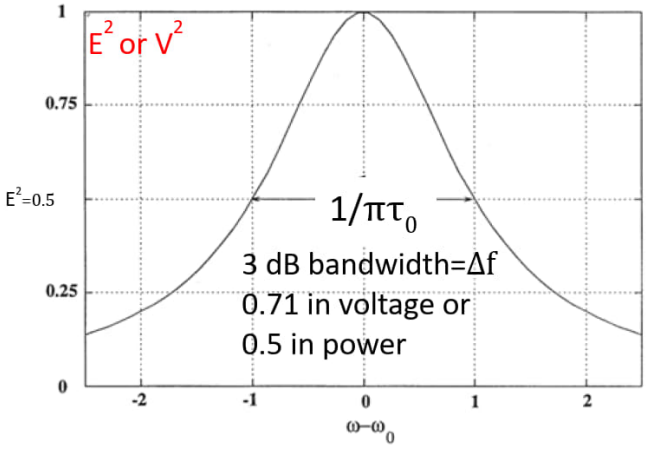

Fig. II.5.11: The 3 dB bandwidth of a resonator and its implications (Image courtesy of Andrea Mostacci).

4.3 Cavity characteristics (pillbox)

The shunt impedance R is given by

$$R = \frac{V_a^2}{2P} \quad , \tag{II.5.17}$$

where V_a is the accelerating voltage, circuit definition (RMS value). The accelerating voltage is the integral of the accelerating field gradient E_a over the cavity active length.

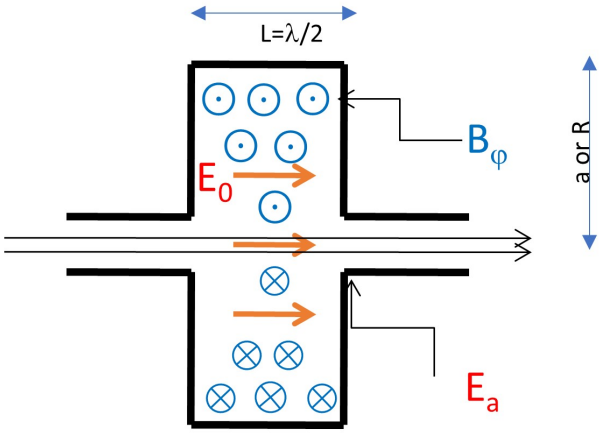

Fig. II.5.12: The axial electric field and the azimuthal magnetic field for a pillbox cavity.

The peak surface electric and magnetic fields constitute the ultimate limit for the effective accelerating field E_a => minimize the ratio E_a/E_0 (don't use the sharp edge for the gap as shown below for the pillbox model in a real cavity) and B_φ/E_0. Note that E_0 is to be taken on the axis of the cavity and B_φ on the equator. Ssee Fig. II.5.12 for the illustration of a pillbox cavity and the main field components, which are described by the following equations (see Chapter II.2 on RF engineering)

$$E_z(r) = E_0\, J_0\left(\frac{\chi_{01}}{R} r\right) \quad , \tag{II.5.18}$$

$$\begin{aligned} H_\varphi \eta &= j E_0\, J_1\left(\frac{\chi_{01}}{R} r\right) \\ &= \frac{j}{\eta} E_0\, J_1\left(\frac{\chi_{01}}{R} r\right) \\ &= j\sqrt{\frac{\varepsilon_0}{\mu_0}} E_0\, J_1\left(\frac{\chi_{01}}{R} r\right) \quad , \end{aligned} \tag{II.5.19}$$

$$H_\varphi \eta = j E_0\, 0.519 \quad . \tag{II.5.20}$$

The ratio between E_0/H_φ is for an ideal pillbox and the E_{010} mode is always $726\,\Omega = 377/0.519\,\Omega$ and independent of L

$$B_\varphi = \mu_0 H_\varphi = \frac{j}{c} E_0\, J_1\left(\frac{\chi_{01}}{R} r\right) \quad . \tag{II.5.21}$$

The equivalence between accelerating field E_a and peak surface magnetic field is for $1\,\mathrm{MV/m} \rightarrow 0.173\,\mathrm{mT}$. Thus, equivalently, $5.78\,\mathrm{MV/m/mT}$.

4.4 R/Q of a pill box resonator

As was discussed in Section 2, the R/Q value of a SRF cavity tends to be favorable compared to a NC cavity, because of larger beam pipes. The R/Q also depends on the full geometry of the cavity, as illustrated in Fig. II.5.13.

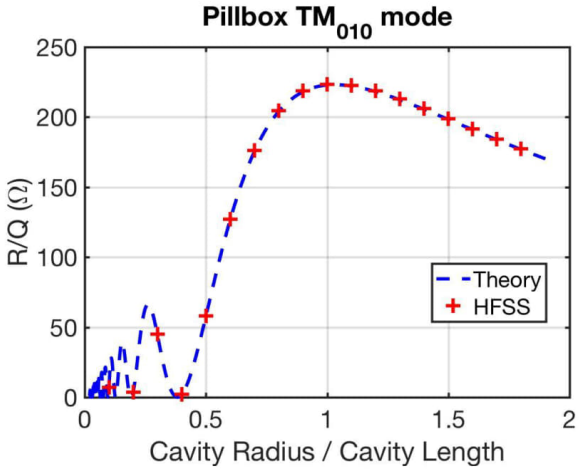

Fig. II.5.13: Visualization of the R/Q value vs. cavity radius R to cavity length L ratio (Image courtesy of Andrea Mostacci).

Quiz: Where is the frequency hidden in Fig. II.5.13? Hint: Use the relation Radius $= 1.53 \times \lambda_0/4$, where λ_0 is the RF wavelength in free space. Resonance condition for the E_{010} mode.

For a relativistic beam (see Fig. II.5.13 which is for $v/c = 1$) we find an optimum when the R/L ratio is around unity. For slow beams the gap must become shorter such that the beam sees not more than half a RF period. For very long cavities with this mode "nothing" happens and very short cavities ($R/L \ll 0.5$) are not close to optimum efficiency; remember, the resonant frequency of this mode (E_{010}) only depends on the radius R.

4.5 Transit time factor

The transit time (TT) factor is the ratio of the acceleration voltage to the (non-physical) voltage a particle with infinite velocity would see [11]

$$TT = \frac{|V_{\text{acc}}|}{\left|\int E_z dz\right|} = \frac{\left|\int E_z e^{j\frac{\omega}{\beta c}z} dz\right|}{\left|\int E_z dz\right|} \quad . \tag{II.5.22}$$

The transit time factor of an ideal pillbox cavity (no axial field dependence) of gap length h is

$$TT = \frac{\sin\left(\frac{\chi_{01}h}{2a}\right)}{\left(\frac{\chi_{01}h}{2a}\right)} \quad , \tag{II.5.23}$$

where χ_{mn} denotes the nth zero of the Bessel function J_m.

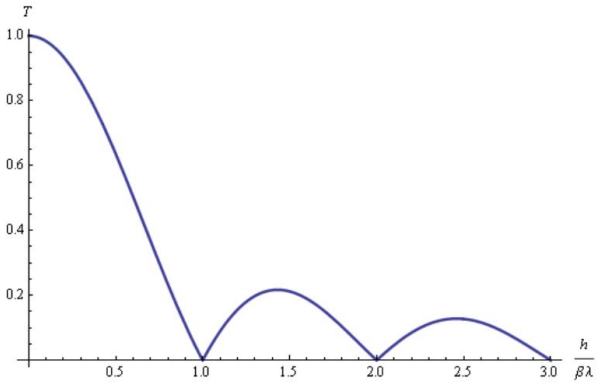

Fig. II.5.14: The transit-time factor for a simple pillbox cavity and a relativistic beam vs. $h/\beta\lambda$ [11], where λ is the free-space wavelength and β is the speed of the particle beam.

Obviously, as shown in Fig. II.5.14, the transit time is best when the gap is very short, but then the particle cannot gain much energy since the interaction length is also short, and we have to find a reasonable compromise between gap length and transit time factor keeping in mind other limitations such as surface electric and magnetic field limitations and also multipactor and heating issues.

4.6 The geometry factor *G* for cavities

The geometry factor is together with the Q-value an important figure of merit for cavities; this is particularly relevant for superconducting cavities. Let's take the surface resistance R_s and we obtain a very simple formula for pillbox cavities (see Fig. II.5.15)

$$G = 453\,\Omega/(1 + \text{radius/length}) \quad , \tag{II.5.24}$$

and also $G = R_s Q$

$$Q = 2\pi f_0 \frac{W}{P_c} = \frac{\omega_0 W}{P_c} \quad . \tag{II.5.25}$$

R_s depends on the material parameters (either NC or SC) including surface roughness, and on several extrinsic properties as discussed above for R_{res} in superconductors, and it is normally assumed constant over the entire surface.

Typical values for G (sometimes also called Γ in literature) are around $270\,\Omega$ for pillbox-like elliptical-shaped cavities (see Section 6.3) used for highly relativistic beams and as low as $20\,\Omega$ for cavities used for slow beams. One may calculate G also with the knowledge of Q in a similar way as the calculation of Q is done via the stored energy in a cavity and the power dissipated per period.

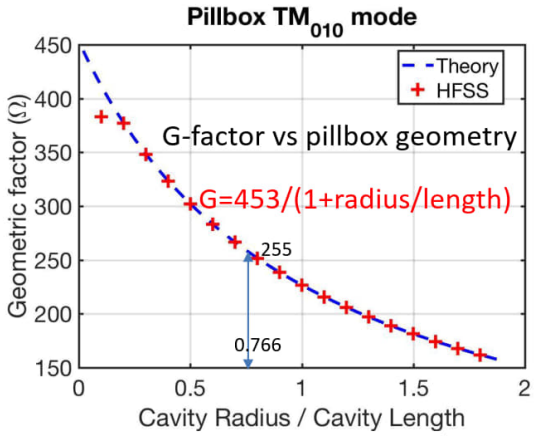

Fig. II.5.15: The geometric factor G of a pillbox vs. R/L ratio (Image courtesy of Andrea Mostacci).

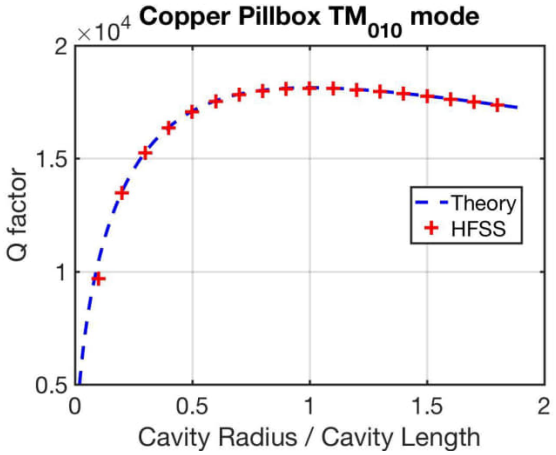

Fig. II.5.16: The Q factor of a pillbox vs. R/L ratio (Image courtesy of Andrea Mostacci).

The geometry factor is more often used for SC cavities, and it is not a direct function of $\beta = v/c$ of the beam, but an indirect one since the shape of the cavity and thus the geometry factor changes as a function of β

$$W = \frac{1}{2}\mu_0 \int_V |H|^2 dV \quad , \tag{II.5.26}$$

$$P_c = \frac{1}{2} R_S \int_S |H|^2 ds \quad , \tag{II.5.27}$$

$$Q_0 = \frac{\omega_0 W}{P_c} = \frac{\omega_0 \mu_0}{R_s} \frac{\int_V |H|^2 dV}{\int_S |H|^2 ds} = \frac{G}{R_s} \quad . \tag{II.5.28}$$

G depends only on the shape of the cavity and is generally calculated numerically with computer codes (MAFIA, URMEL, HFSS, CST, etc.), and does not contain the transit time factor. On the other hand, R/Q contains the transit time factor.

For an ideal "pillbox" cavity that maximizes Q_0 (see Fig. II.5.16) G is e.g. $257\,\Omega$. For an accelerating cavity for relativistic particles ($\beta = 1$) like those used at CERN, G ranges in $270/295$ ohm. The Q_0 factor of a SC cavity is in the $10^9/10^{10}$ range!

Quiz: Relation between Q and G, where G is the geometry factor and depends only on the geometry, not on the material. At resonance: $a = 0.383\lambda$ and if $L = \lambda/2$ we get $G = 453/1.766 = 257$.

Keep in mind that for SC cavities, the unloaded Q is quasi-infinite compared to the loaded one.

Our cavities are meant to accelerate particles, and the accelerating electric field on axis is of basic importance. However, most of the considerations on the surface impedance are based on the surface magnetic field and on the induced currents.

For a given geometry, there exists a fixed proportionality between B_0, E_0, and E_{acc} as seen in Tab. II.5.1, and as also mentioned in Section 4.3.

Table II.5.1: Comparison of magnetic surface field vs. electric accelerating field for different cavity shapes.

	"Pillbox"	Elliptical
B_0/E_{acc} [mT/(MV m)]	$3.68 = 5.78 \times 2/\pi$	4.55 (example)
E_0/E_{acc}	$\pi/2$	2.3 (example)
$G\,[\Omega]$	257 (ideal pillbox with $L = \lambda/2$)	295 (example)

4.7 Summary for cavity basics and learning targets

- The pillbox resonator (TM_{010} mode) allows – as a paradigm - the analytical description of typical accelerator parameters, such as peak surface fields (E and H), power loss and Q-value, shunt impedance, geometry factor, etc.
- "Real" accelerator cavities are designed by making use of computer codes such as CST Studio Suite, HFSS, COMSOL, MAFIA, SUPERFISH, etc.

– The response of a cavity to an RF signal (CW or pulsed) from a generator is well described by lumped circuit networks, in particular for the transmission and reflection of an electromagnetic wave on this device.
– A relation between the surface magnetic field on the equator of an ideal pillbox and the electric field on axis is derived and discussed; This ratio tells us how much accelerating field we get until we hit the B-field limit in SC cavities .
– We also introduce and use the geometry factor G which is relevant for SRF but less important and less used for NC cavities.

5 RF diagnostics

5.1 How to measure the RF surface impedance of samples

Normally, some kind of dedicated resonator is used for measuring samples. You must avoid, if possible, any (sliding) contacts since they have usually an undefined contact resistance and spoil the Q of the cavity and you should avoid any radiation losses (radiating apertures). Often a TE_{011} mode type resonator is used. It works very well, it is not sensitive to contact resistance between the tube and the end plates due to azimuthal wall current only (entire resonator) and no currents passing over the "end plate to cavity body" contact. But if you would like to go to lower frequencies then the quadrupolar resonator is a good choice. For even lower frequencies the shielded two-wire coaxial resonator has been used (for the LHC beam screen). The presence of dielectric material in the test resonator can significantly spoil the Q value; try to minimize its volume and/or place it in a region of vanishing electric field, or use an excellent dielectric with low losses like sapphire.

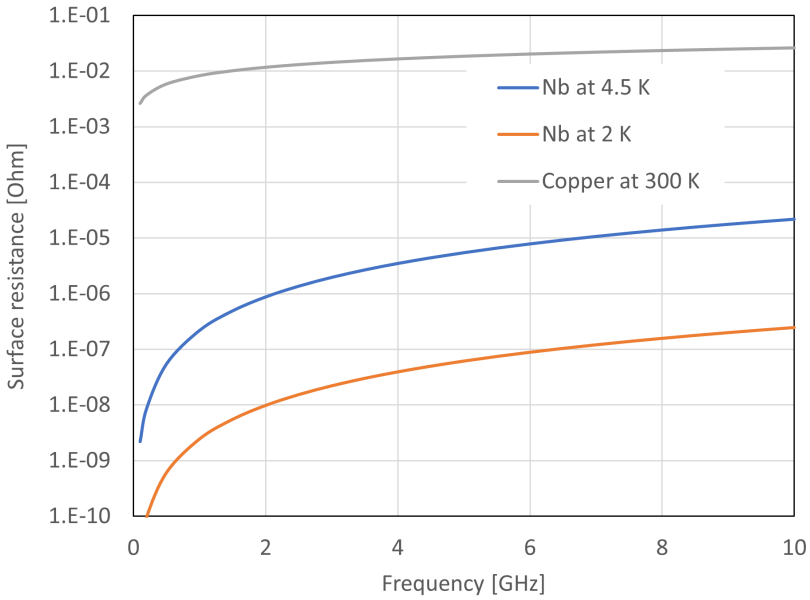

Fig. II.5.17: Comparison of surface resistance vs. frequency for copper at room temperature and niobium at different temperatures.

Why is it good to use a TE_{011} mode pillbox cavity?

There are no wall currents in the longitudinal direction and the mode is cylindrical symmetric and thus the setup is insensitive to the contact resistance of the removable end-plate or flange. Caveat: mode degeneracy.

Figure II.5.18 illustrates the surface currents inside the cavity: azimuthal surface current density which is equal to the longitudinal or radial (cover plates/flange) B-field respectively.

Quiz:

- Can you guess or find out from the normal conducting RF lecture which mode will degenerate with the TE_{011} in the pillbox?
- What could be a simple measure to break this degeneracy?
- How would you design a coupler for the TE_{011} mode?
- What is the orientation of the RF surface current related to the RF surface magnetic field (parallel or orthogonal)?
- Is the RF surface current of the endplate radial or azimuthal for the TE_{011} mode?

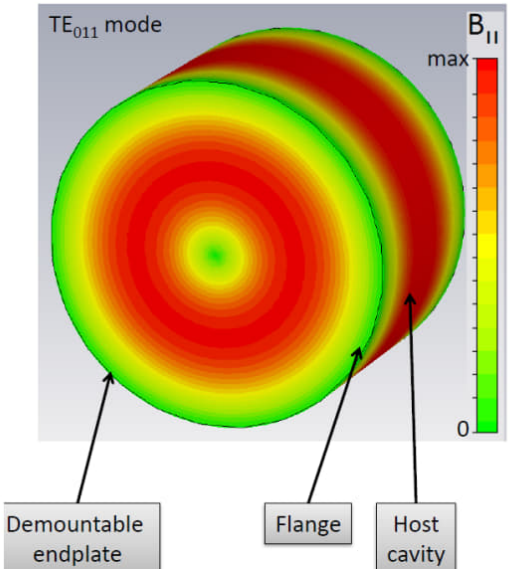

Fig. II.5.18: The pillbox in the TE_{011} mode with demountable end plate for material properties measurement [12].

Here is the answer to the question on degeneracy (since this is not so trivial): The TE_{011} (or H_{011}) mode is degenerate with the TM_{11} or (E_{111}) mode; H_{01} and E_{11} are already degenerate (i.e. same cutoff frequency) as waveguide modes in the circular waveguide.

The substitution method technique shown in Fig. II.5.19 is used when the relative change (from the test sample) of the total Q of the test cavity is rather small (e.g. quadrupolar resonator, see Fig. II.5.20) and thus the measurement results become uncertain.

The procedure is the following: start at a rather low temperature of the bath, then turn on some DC power ($P_{\mathrm{DC},1}$) until the bath temperature of interest is reached; turn on the RF and reduce the DC power to $P_{\mathrm{DC},2}$ to keep the bath temperature constant (reducing the known DC power by the amount of

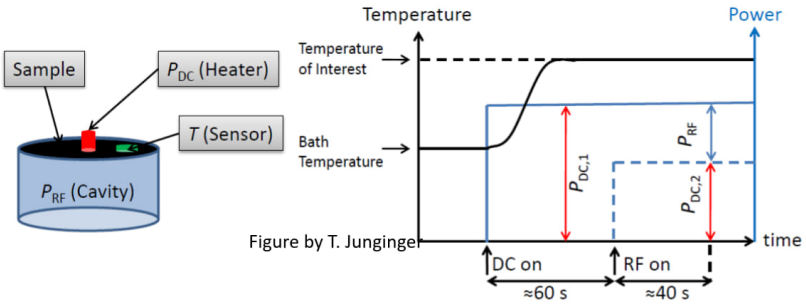

Fig. II.5.19: Evaluation of RF surface resistance with the DC substitution method [12].

unknown RF losses and then calculate the R_s from the power difference). This amounts to a calorimetric evaluation of Q_0.

What happens here exactly? Why do we turn the DC on? For calibration try to stay constant at the "temperature of interest" and then when the RF comes ON the DC power is reduced accordingly to keep the temperature of interest at the same level, thus getting this way the RF losses.

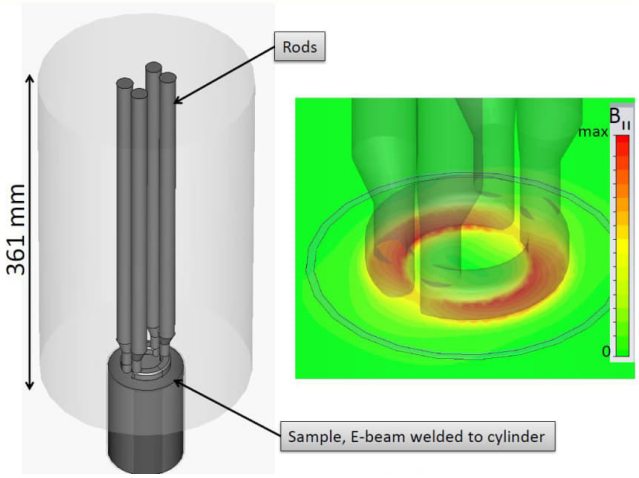

Fig. II.5.20: The quadrupolar rod resonator for contactless measurements and its field pattern [12].

Quiz: Why should we use the resonator from Fig. II.5.20 when we have the nice TE_{011}-type pillbox?

Answer: it allows for lower frequencies or a smaller sample size compared to the pillbox resonator. Note, that the eddy currents induced in the sample are only local ("focused") and don't pass over contacts. This setup is still (2024) in operation at CERN. The purpose is to avoid contact with the sample because contact resistance is always a big mess, and hard to control.

The configuration shown in Fig. II.5.21 was used for more than 15 years until someone said: "We do not need it anymore let's scrap it". And three years later it was resurrected and re-built from scratch.

This setup has been intensively used for measurements of the normal conducting copper losses of the LHC beam screen at cryo temperature with a strong static magnetic field; it is now again rebuilt for

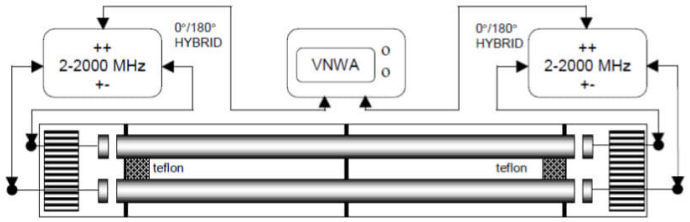

Fig. II.5.21: The shielded parallel wire resonator for material measurement at cryo and with magnetic field. Note that the direction of the static B-field is orthogonal to the axis of both rods but 30 °C inclined to the plane defined by the axis of the two rods due to practical constraints of the measurements setup [13].

the FCC beam screen evaluation which may have high T_c superconducting coating (compatible with the strong DC magnetic field). The static B-field is transverse to the axis of the resonator or beampipe.

5.2 Test set-up for an existing SC cavity

Let us start from scratch with a "Gedanken experiment" (or kind of quiz if you like). Since the cavity has a very high unloaded Q value we cannot use the conventional method to measure the 3 dB bandwidth in transmission or in reflection with a network analyzer (VNA): why? The expected 3 dB bandwidth (practically unloaded Q) would be in the ballpark of 1 Hz maybe even much less. Imagine what happens if you try measuring this with a VNA. Measurement time, stability, frequency resolution of the VNA (you would need a few mHz step size).

Someone proposed (and there are related papers): just make the cavity oscillate via feedback and once it is in a stable state open the feedback loop and measure the decay in the time domain. This works and has also been applied, but you cannot easily control the power level in the cavity this way. Thus, it is better to use an external generator with a PLL (phase-locked loop circuit) that tracks the actual frequency of the cavity under test (such a cavity is never really stable to a fraction of a Hz in a helium bath). The power of the external generator can nicely be adjusted to any amplitude level (to get the field-dependent measurement of Q value vs. E_{acc}). From the exponential decay (exponential if the cavity is linear: what does this mean?) one can easily calculate the Q.

Quiz: What other arguments can you find not to measure the unloaded Q value for numbers $> 10^9$ in the frequency domain with a VNA?

In many cases since SC cavities are usually operated strongly over coupled it is nicely possible to measure the loaded Q (in transmission) but in order to deduce the unloaded Q from this measurement a precise knowledge of the coupling factor beta is required which is often not trivial.

5.3 Measuring setup for Q values of SC cavities

These days mostly the self-excited setup is used. A highly simplified circuit diagram is shown in Fig. II.5.22, we need in reality a few more items like a bandpass filter for mode and frequency band selection, some electronic switches to see how the RF field decays, and also some diagnostics (RF detector/scope etc).

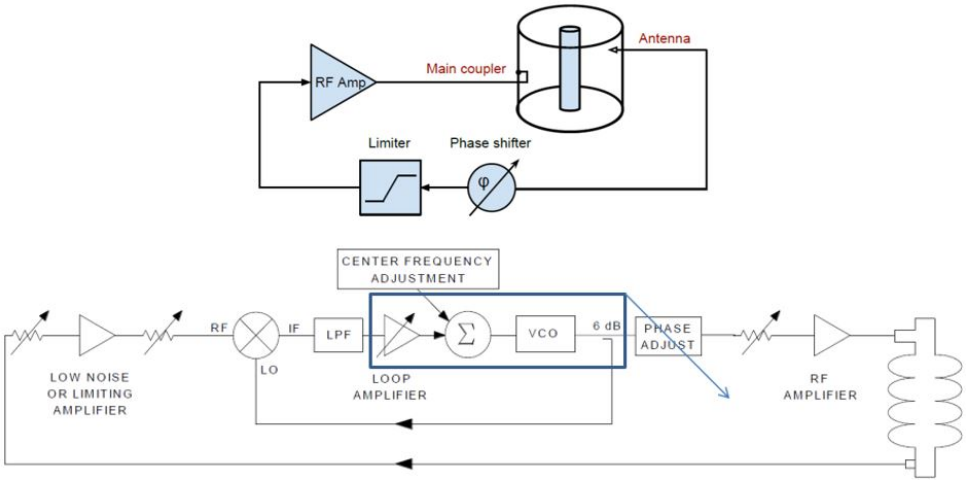

Fig. II.5.22: The self-excited superconducting cavity for Q measurements, basic circuit; technical details of the test circuit [14].

Quiz: Why not simply use a Vector Network Analyser as normal for NC cavities?

And for comparison, the real setup diagram of the PLL method is shown in Fig. II.5.23.

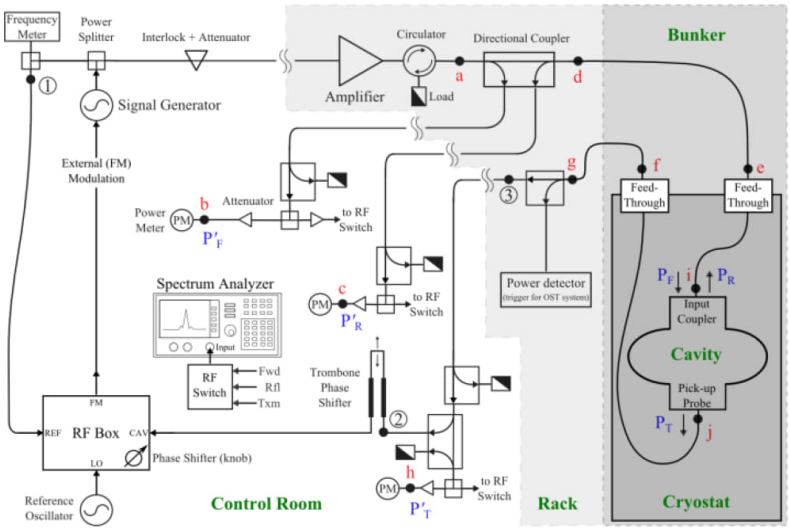

Fig. II.5.23: Complete circuit diagram for a SC cavity Q measurement [14].

The examples shown so far are by no means exhaustive.

For the design of new measurement setups e.g. related to the evaluation of surface roughness impact, one may have to take anisotropy issues into account, depending on the structure of the surface roughness (e.g. laser erosion for multipactor reduction). For very high frequencies, confocal resonator (Fabry-Perot type) setups were used. A Fabry-Perot is also known as a confocal resonator. For tube-like (beam-pipe style) samples, the first resonance frequency is often too high to cover the frequency range of interest. In this case, one may insert a sapphire rod which at cryo has extremely low RF losses and a

dielectric constant around 10 (caveat: anisotropic).

This type of measurement has a lot of “caveats”.

5.4 Recent measurement layouts and examples for other SC resonators

The examples of Fig. II.5.24 are for high-purity aluminum which has excellent RRR at very low temperatures.

Reference [15] gives a nice overview of recently developed and applied resonator-based measurement methods. It is really recommended for further reading.

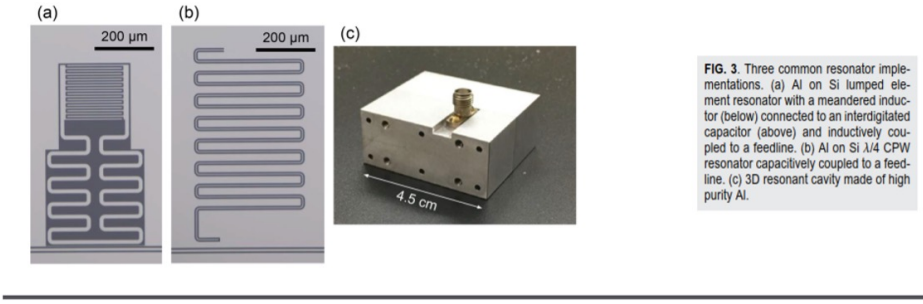

Fig. II.5.24: Test resonator for RRR measurements on aluminum at very low temperatures [15].

The setup shown in Fig. II.5.25 is for measurements at really very low temperatures ($15\,\mathrm{mK}$). A comparable version is in operation in Korea (CAPP) for axion research. In this case, the NC cavity (at deep cryo to enhance the Q_0 and reduce the thermal noise) is the actual axion receiver. Caveat: axion cavities are operated in a strong DC magnetic field which is not compatible with conventional superconductors, but works well with High-Temperature Superconductors (HTS).

5.5 Learning targets

After having worked through this chapter and the lectures on basic SC it would be nice if you could:

- Be familiar with the motivation for using RF superconducting cavities in accelerators;
- Be able to discuss why SC RF cavity technology is barely used outside the accelerator field;
- See the benefits but also the problems related to RF SC technology;
- Have understood the main difference between DC and RF superconductivity;
- Be able to calculate the RF surface impedance of a given material (NC and SC) vs. frequency;
- Have understood the concept of the resistance and impedance per unit square;
- Be able to name some of the materials used for RF SC applications;
- Have understood the principal difference between conventional RF superconductors and high-temperature RF superconductors;
- Be familiar with the basics, history, and some important milestones of superconducting RF technology in general (see Fig. II.5.3);

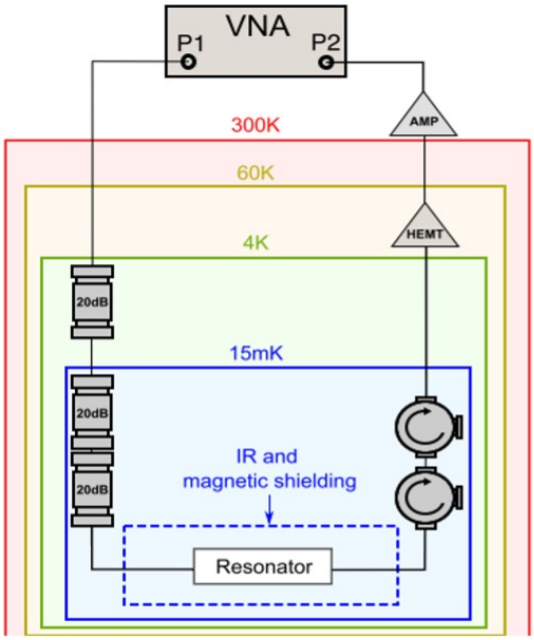

Fig. II.5.25: Measurement layout for tests below 20 mK [15].

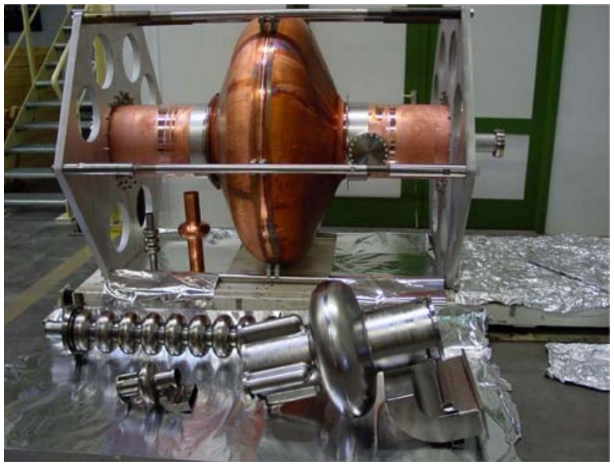

Fig. II.5.26: A collection of superconducting cavities [16].

– Have some ideas (and be able to give examples) on how to measure the surface impedance of RF superconductivity.

6 SC cavity implementation

6.1 Real examples of RF cavities

In Fig. II.5.26 the big object is a single-cell 200 MHz copper cavity niobium coated inside: the niobium film is typically deposited by sputtering. This technology was developed for LEP at CERN and is now mostly used for cavities for circular colliders and some low-energy heavy-ion linear accelerators, which use low-frequency cavities. This technology allows considerable cost-saving compared to the bulk nio-

bium technology. In the foreground, some smaller bulk-niobium multiple and single-cell cavities with different frequencies and different sizes can be seen. Details on fabrication are discussed in Section 9. In this photo, cavities go from 200 MHz up to 3 GHz and often one talks about "elliptical" cavities; but this does not mean that those cavities have an elliptical cross-section (although this exists, see 6.3).

6.2 Electron multipacting

In the old days, superconducting cavities had a rather rectangular longitudinal cross-section (left side of Fig. II.5.27), easy to fabricate, but which resulted in strong first and second-order (2-point) multipactor, limiting the usable field strength to a few $\mathrm{MV/m}$. After many years of experimental numerical and theoretical work, the Gaussian or bell shape form with the ellipse as an asymptote in the transition region (right side of Fig. II.5.27) was found [17, 18]. Learning by doing. This is sometimes a boring and tedious job.

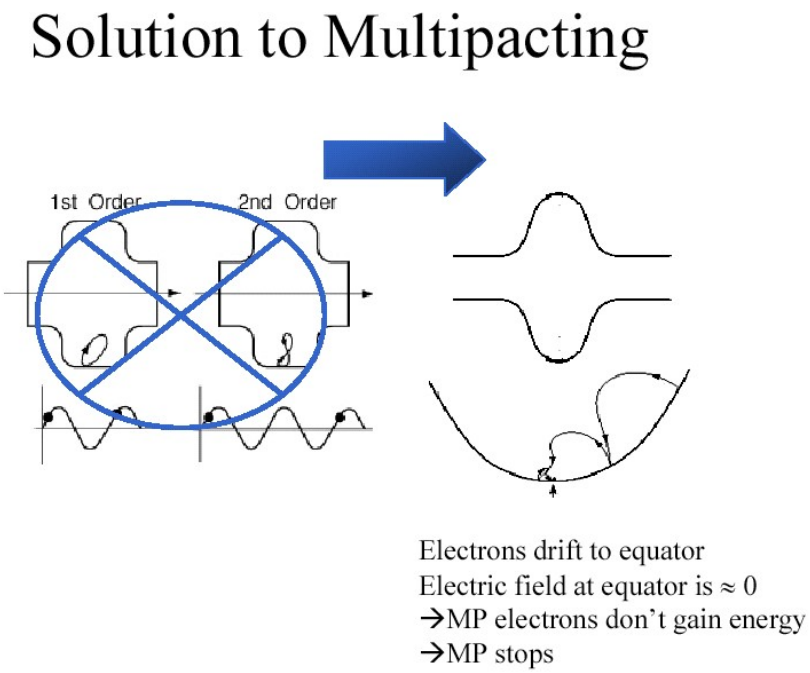

Fig. II.5.27: Evolution of the SC cavity shape driven by multipacting issues [19].

Not only is multipactor limiting performance by absorbing RF energy. In a superconducting cavity, localized heating by multiple impacts from electron current due to secondary emission in resonance with RF field may even bring the cavity wall above critical temperature, leading to a "quench". Historically this phenomenon was a severe limitation for the performance of SC cavities. The invention of the "circular" shape (in the region of the equator) opened up the avenue for higher gradients. Usually squared boxed shapes favour resonant multipacting, thus round and elliptical are preferred [20].

6.3 What are elliptical cavities?

The term "elliptical" (see Fig. II.5.29) refers to the particular shape in the longitudinal cut of such a cavity which had been found over many years of optimization in order to mitigate two-point multipactor inside

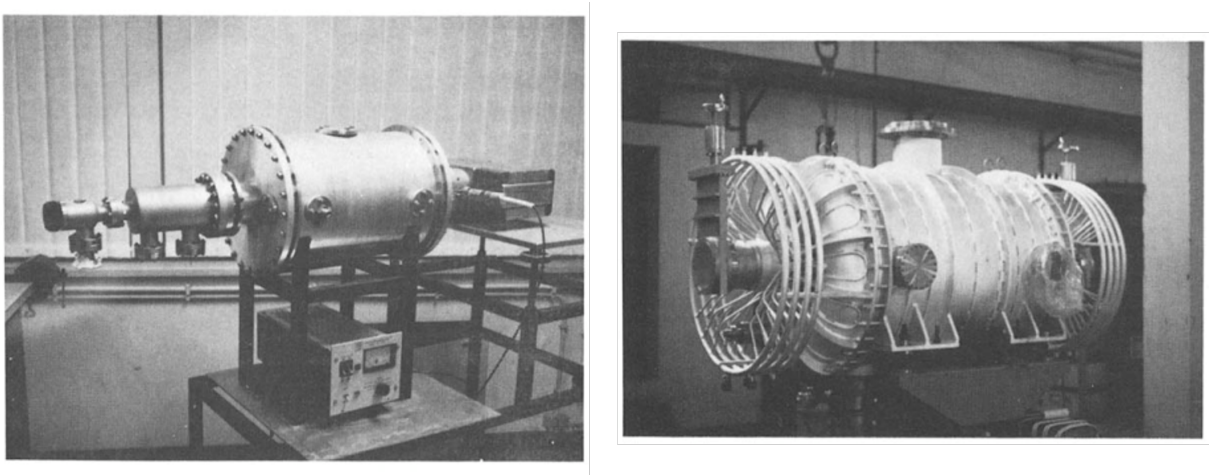

Fig. II.5.28: The evolution path towards the nowadays-used bell-shape. In this historical image we see the change from boxed-type (left) to rounded shape (right) that first allowed suppression of multipacting [20] (see also Fig. II.5.27).

such types of cavities. Two-point mutipactor is the resonant multiplication of electrons inside a cavity: electrons are field-emitted from some surface defect, accelerated, and impinge on a facing surface, where they are multiplied if the secondary electron emission yield (SEY) coefficient is larger than unity (which often is, at electron energies < 1 keV). Re-emitted electrons are accelerated back to the original emission point, and multiplied again, and so on, absorbing RF energy from the cavity. The "elliptical" shape (longitudinal cut) is characterized by the asymptotic ellipse in the transition region from the beampipe to bell-shaped cavity form and also near the equator.

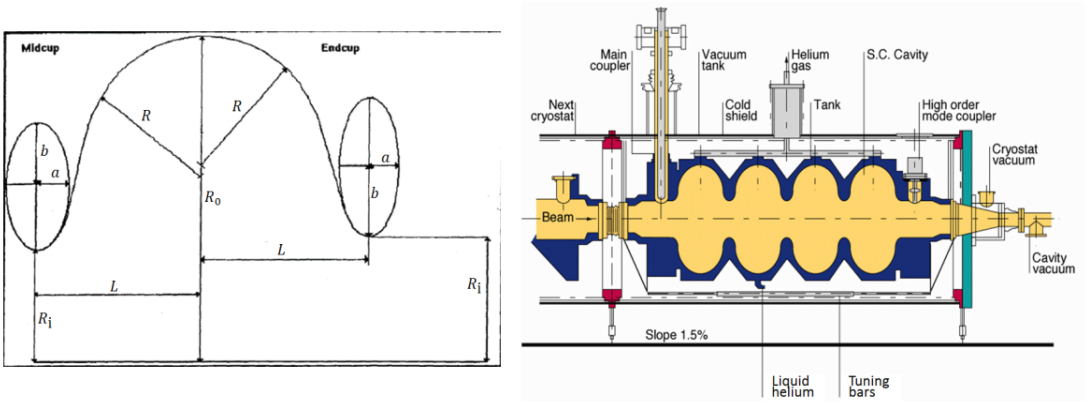

Fig. II.5.29: Why is this cavity shape called "elliptical" [21, 22].

6.4 A typical storage ring cavity (LEP)

In Fig. II.5.30 we can see a bulk niobium and a niobium-coated copper cavity of LEP (there were 16 bulk niobium and 272 Niobium-on-Copper cavities in LEP), electron-beam welded, 352 MHz. It is noted that the long ports are for the main couplers, short ports for the HOM couplers, and diagnostics (field probes).

Fig. II.5.30: Top: bulk niobium cavity of LEP [23]. Bottom: niobium-coated copper prototype (Image courtesy of CERN).

6.4.1 Integration into LEP cryostat

The LEP cryostat could reliably be operated under CW conditions with a beam and in pulsed conditions without a beam in the present LHC tunnel environment (1.4% slope= inclination of the plane of the ring). It is worth noting that the liquid He tank, the gas openings, and He collector were relatively small.

Pulsed operation: the thermal diffusivity $k = \lambda/(c\rho)$ is such that it takes $\sim 1\,\mathrm{ms}$ before the temperature pulse arrives at the niobium helium interface => advantage compared to CW operation.

This cryostat was tested under pulsed conditions with a beam in the CERN SPS. It's the sum of many elements that have to work properly together, and the chain is likely to rupture at the weakest point. The integration of the actual cavity into the vacuum vessel is a major task (see Fig. II.5.31). They have to be taken into account: low heat loss, cryo cooling, maybe tuners, all sorts of diagnostics, RF probes, the main coupler, etc.

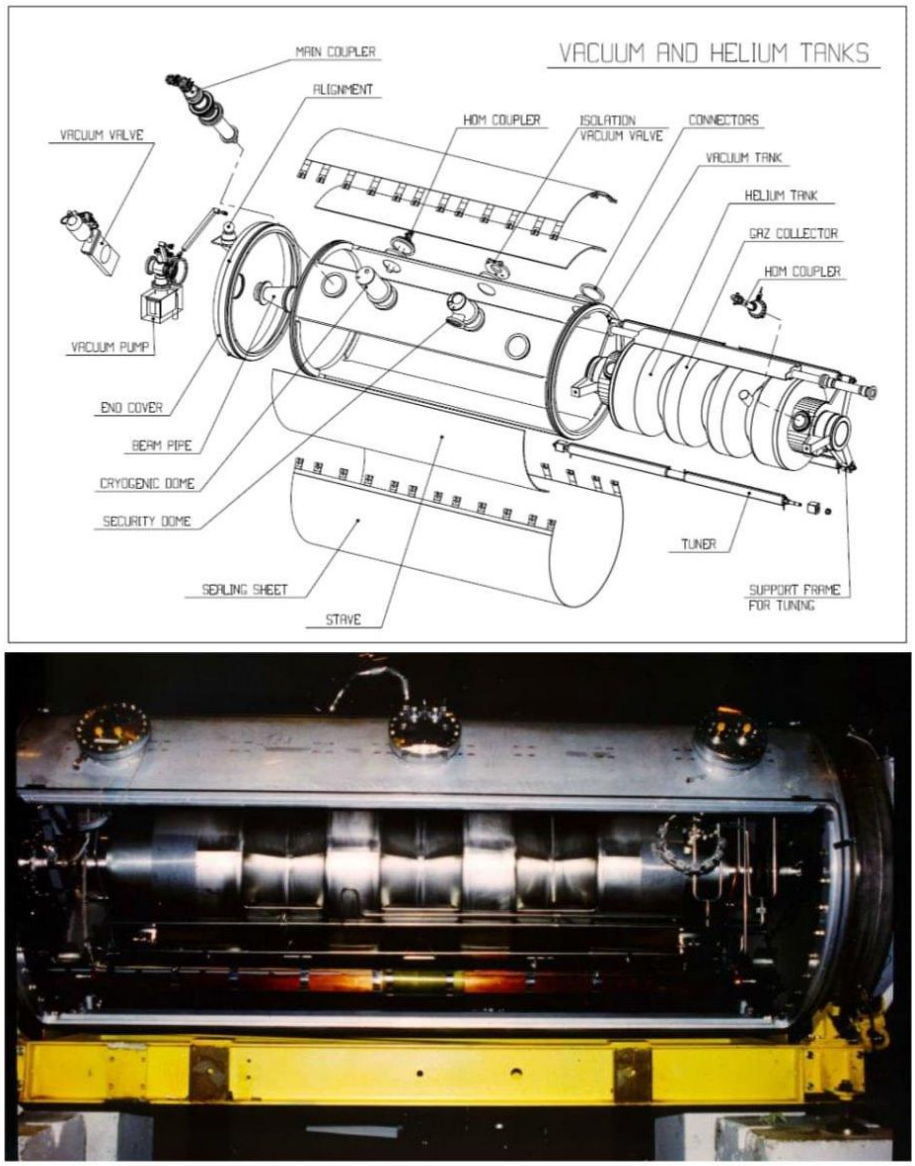

Fig. II.5.31: The integration of the cavity into the cryostat. Top: exploded view. Bottom: photo (images courtesy of CERN).

6.4.2 Cryomodules LEP installed in the tunnel

Do you notice the rather flat waveguides for about 350 MHz in Fig. II.5.32; there would have simply been no space for the normal aspect ratio (around 1 to 2).

Quiz: Can you estimate the length of the larger size (width) of the waveguide?

Installation of this type of waveguide in the tunnel can be very delicate (see Fig. II.5.32). ESS (Lund) knows that really well. Thus, give it enough mechanical margin for waveguide installation.

6.5 CERN - LHC cavities

These cavities are conceptually similar to LEP cavities, slightly differing in frequency and in the number of cells. They were designed and fabricated soon after the LEP cavities, exploiting the same production

Fig. II.5.32: LEP cryomodule (352 MHz) installed in the tunnel [24].

Fig. II.5.33: 400 MHz SC cavities in the LHC (former LEP) tunnel [25].

chain: they were probably the very first new accelerator component built for the LHC

- $f_{\text{res}} = 400\,\text{MHz}$,
- $R/Q = 45\,\Omega$ (using circuit definition),
- $Q_0 = 2 \times 10^9$,
- $E_{\text{acc}} = 5.33\,\text{MV/m}$,
- $P_{\text{in}} = 116\,\text{kW}$ (CW) to be transferred to the beam,

Fig. II.5.34: LHC cavity after Nb thin film coating by sputtering (Image courtesy of CERN).

– Niobium-film on Cu with $1\,\mu\mathrm{m}$ to $2\,\mu\mathrm{m}$ thickness, deposited by by sputtering, Fig. II.5.34.

In Fig. II.5.33, there are four single-cell cavities per cryomodule where each resonator delivers $2\,\mathrm{MV}$, has a Blade tuner (detail discussed later), "Doorknob" power coupler, $75\,\Omega$ coaxial shown on another section (air cooled in cryo). Can you guess the purpose of the blue hose ending above the waveguide top of the cavity? There are in total 8 cavities per beam, therefore $16\,\mathrm{MV}$.

6.6 XFEL – DESY

The XFEL-DESY cavity is shown in Fig. II.5.35

– $f_{\mathrm{res}} = 1300\,\mathrm{MHz}$,
– Standing wave; elliptic,
– RRR 300 Niobium,
– TM_{010} π-mode,
– active length is $1.038\,\mathrm{m}$,
– $Q_0 > 10^{10}$,
– Iris diameter is $70\,\mathrm{mm}$,
– Nominal gradient is $23.6\,\mathrm{MV/m}$,
– Cell to cell coupling $K = 1.87\%$.

6.7 CEBAF – JLAB

In Fig. II.5.36 we see the different production stages of those SC cavities. First, half-shells are required for each cell. Then, waveguide port couplers. One waveguide for the RF-in, and the other one for HOMs–out.

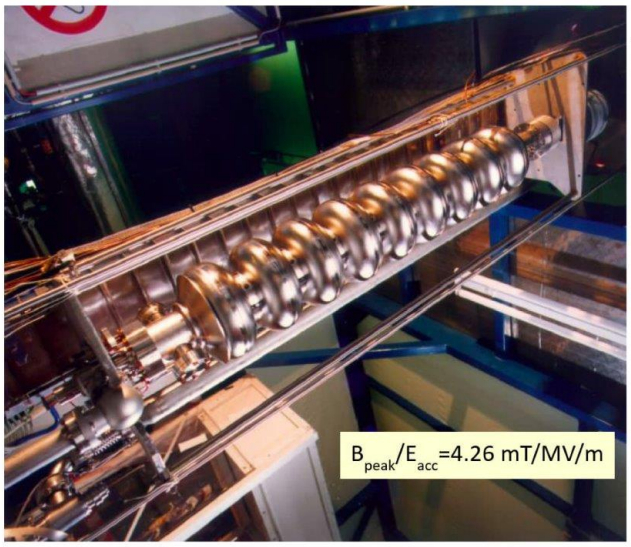

Fig. II.5.35: The XFEL-DESY cavity [26].

Fig. II.5.36: A collection of cavity shapes and building blocks (Image courtesy of Research Instruments).

Note that practically all SC multiple-cell cavities are operated in the standing wave mode (in contrast to NC multiple-cell cavities which are often in traveling wave mode and some of them in forward traveling wave mode, and some use backward waves. This (traveling wave) allows more bandwidth and is also applied for heavy beam-loading.

6.8 SNS and ESS (moderate beta examples)

Spallation Neutron Source (SNS) in Oak Ridge (TN) and European Spallation Source (ESS) in Lund (SE) are two linear proton accelerators operating as neutron spallation sources, and both rely upon SRF cavities to accelerate MW-class proton beams over a target (mercury in the case of SNS, and a rotating lead target in the case of ESS) and produce neutrons.

In Fig. II.5.37 we see some low-β cavities from the SNS, while in Fig. II.5.38 we see the three families of SRF cavities from ESS.

Fig. II.5.37: The SNS $\beta = 0.61$ and $\beta = 0.81$ cavities [27].

Quiz: What is characteristic of moderate or low $\beta = v/c$-value cavities?
A: The bell shape of a cell?
B: The shorter gap compared to $\beta = 1$ cavities?
C: The diameter?

Fig. II.5.38: The three different ESS cavity families: low-beta $\beta = 0.5$ two-spoke cavity (top left, courtesy IJC Lab), the 6-cell elliptical medium-beta $\beta = 0.67$ cavity (top right, courtesy INFN-LASA, and the 5-cell elliptical high-beta $\beta = 0.86$ cavity (bottom, courtesy CEA).

6.9 Heavy ion accelerators (low beta examples)

In Fig. II.5.39 we have excitation via tank probe or "loop antenna". This type of spiral resonator is also known as split ring resonator: 97 MHz and 145 MHz $\beta = 0.06$ to 0.16.

Fig. II.5.39: Spiral resonator SRF cavities from ATLAS-ANL (note the lead plating inside the cavity copper body) [28].

This is the superconducting version of a cavity with a similar shape (but normal conducting) developed at GSI in the early 80ies. This type of structure is suitable for slow beams and has a very high shunt impedance.

Quiz: How would you design the water cooling for the NC resonator coil?

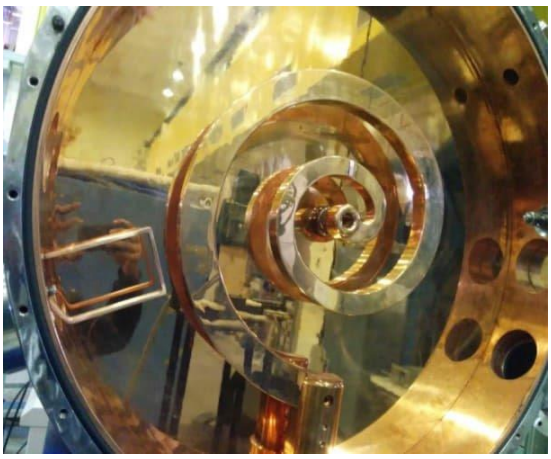

Fig. II.5.40: Spiral resonator NC, for comparison [29].

In Fig. II.5.40 we see a 48.5 MHz spiral resonator (MEBT).

Some further shapes of heavy ion accelerator SC cavities with low β are shown in Fig. II.5.41. Note that for low-β beams there are often two gaps to pass for the beam while the sign inverts during the passage of the slow beam through some hole on the resonator like a drift tube.

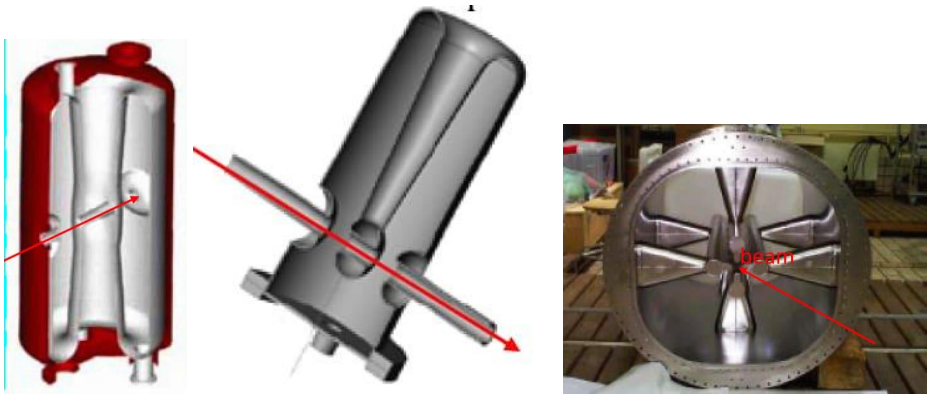

Fig. II.5.41: Different shapes of low β SC cavities including an RFQ at the right [30].

6.10 Shape versus β

We know that for a relativistic beam, the gap length should be $< \lambda_0/2$, since then the particle sees a half-wave.

Example: 300 MHz; $\beta = 1$, $\lambda = 1\,\mathrm{m}$. A good gap length considering also R/Q is $\approx 40\,\mathrm{cm}$ and $> 50\,\mathrm{cm}$ leads to cancellation.

The change in the cavity shapes for different β requirements are shown in Fig. II.5.42.

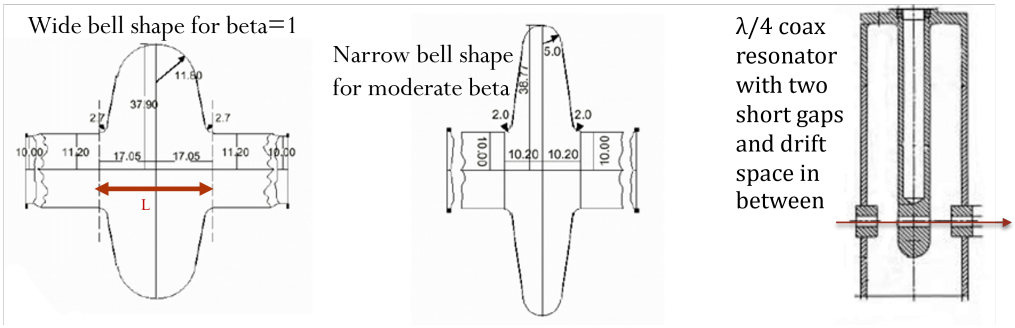

Fig. II.5.42: Change of shape vs. β. The gaps are getting smaller and smaller for low β [31].

Some typical SC cavities' parameters for different accelerator types are shown in Tab. II.5.2.

Table II.5.2: Some typical parameters of SC cavities in different types of accelerators.

Electron accelerators	**Proton accelerators**	**Ion Accelerators**
$\beta \approx 1$	$\beta \approx 0.5$ (moderate β region)	$0.05 \leq \beta \leq 0.2$
$350\,\mathrm{MHz} \leq f_0 \leq 2\,\mathrm{GHz}$	$500\,\mathrm{MHz} \leq f_0 \leq 1.5\,\mathrm{GHz}$	$50\,\mathrm{MHz} \leq f_0 \leq 150\,\mathrm{MHz}$
$G \approx 270\,\Omega$ (geom. factor)	$G \approx 170\,\Omega$ (geom. factor)	$G \approx 20\,\Omega$ (geom. factor)
$L \approx 35\,\mathrm{cm}$ ($f_0 = 350\,\mathrm{MHz}$)	$L \approx 20\,\mathrm{cm}$ ($f_0 = 350\,\mathrm{MHz}$)	$L \approx 5\,\mathrm{cm}$ ($f_0 = 150\,\mathrm{MHz}$)

6.11 Some deterministic parameters for cavity performance

Until now we discussed the role of the RF frequency, the He bath temperature, and SC material with its characteristic critical field and temperature. There are still other (less important) parameters that determine the performance of the cavity as well (see Tab. II.5.3).

Table II.5.3: Deterministic parameters for cavity performance.

Influencing quantity	Impact quantity	Physical explanation	Cure
External static magnetic field B_{ext}	Residual surface resistance	Creation of vertices	Shielding of the ambient magnetic field by Mu-metal / Cryoperm
Residual resistivity ratio RRR	BCS surface resistance	Mean free path dependence of R_{res}	Annealing steps during ingot production/after cavity manufacture
Ratio peak magnetic field to accelerating gradient B_p/E_a	Max. accelerating gradient	Critical magnetic field as ultimate gradient limitation	Optimization of cavity shape
Nb-H precipitate	Q-value / acc. gradient (Q-disease)	Lowering of T_c/B_c at precipitates of Nb-H	T-control during chemical polishing Degassing at 700 °C Fast cool-down

7 Interaction of cavity-beam

We are now going into more detail about cavity beam interactions and vice versa. As already mentioned usually the cavity is used as a transformer to convert the available generator power into as much as possible voltage seen by the beam. However, each cavity is acting simultaneously as pickup and kicker and the beam-induced voltage and thus power can lead to surprising side effects.

7.1 Passband modes in multiple cell structures

A nice simple illustration of the RF modes in multicell cavities is shown in Fig. II.5.43, the relative phase of the different modes should be self-evident to the attentive reader (possible phase shifts are equal to the number of cells). Modes are coupled through the ports between cells, and the resulting coupling constant has the same role has a coupling between two pendulums as illustrated in Fig. II.5.44, hence the discrete phase shifts: if the pendulums are not in discrete phase ratios, there is no resonance (chaotic movement), as in cavities.

7.2 Intuitive introduction: the surfer

As shown in Fig. II.5.45, surfing on the waves means staying in synchronism. In particular, this is important for multi-cell cavities and of course, this also applies to NC multiple-cell cavities or when you do this on a nice warm summer day near Hawaii or just on the Mediterranean. Contemplate the difference between “deeply thinking” and “deeply sinking”.

7.3 Reasons for beam induced mechanical oscillations - radiation pressure

Note that this “radiation pressure” is not always a pressure trying to “inflate” the cavity; in reality, it is rather a position-dependent deformation (see Fig. II.5.46). As an analogy, the plates of a charged capacitor are attracted, and conductors with parallel currents repel each other.

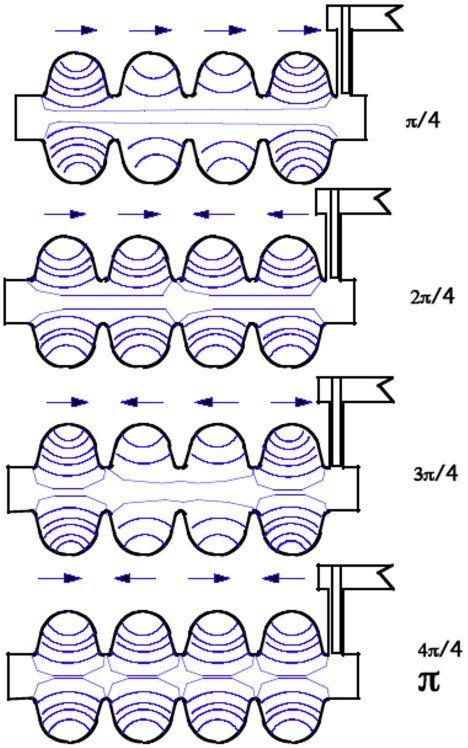

Fig. II.5.43: Comparison of cavity field patterns [31].

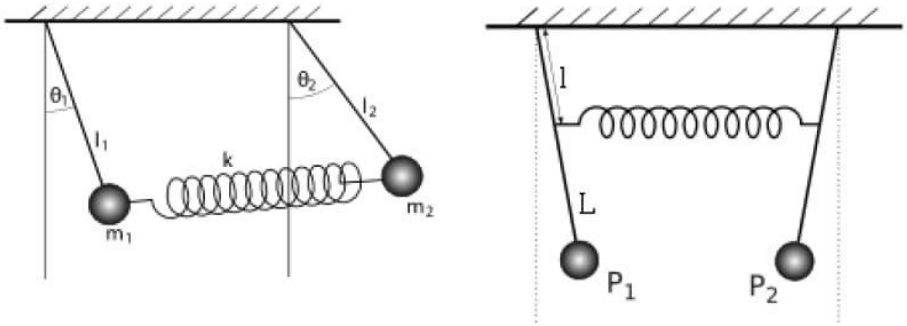

Fig. II.5.44: Examples of coupled pendulums [32].

7.4 Mechanical oscillation modes

For example, at LEP, a radiation pressure on the cavity walls of about 1000 N in total is possible. It's essentially the batch pattern that reduces periodically the field strength (beam loading) and if this hits a mechanical resonance we may get a problem. The frequencies are usually on the order of a few 10 Hz to several hundred Hz (see Fig. II.5.47).

7.5 A fast frequency tuner

We need a rather fast frequency tuner (plunger is tricky) to compensate for those oscillations in the audio range. The type of plunger seen in Fig. II.5.48 may be good for slow tuning (say below 1 Hz) but not easy to operate at say 30 Hz, for fast tuning (beam-induced vibrations via "radiation pressure" from the

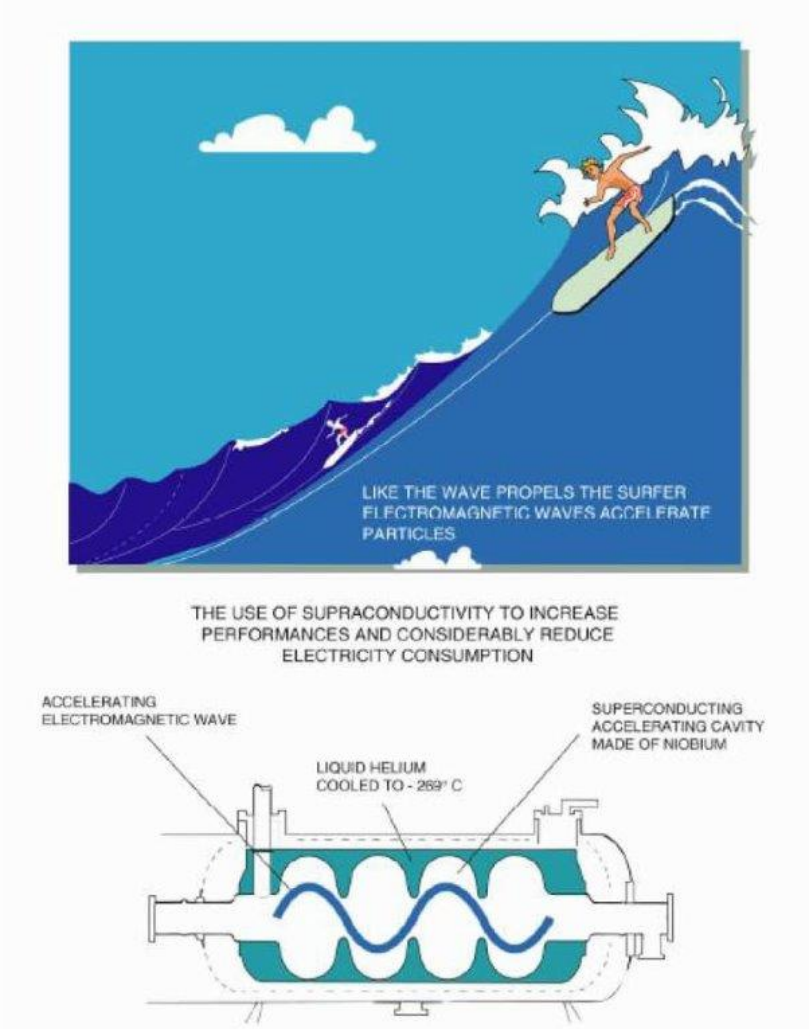

Fig. II.5.45: The donkey and the carrot ensure that the electron always sees an accelerating field [31].

time-dependent envelope of the field in the cavity via batch structure) we need piezo or magnet-restrictive tuners with up to kHz bandwidth.

The frequency variation is linked to the change in electric and magnetic field distribution inside the cavity, due to geometric deformations:

$$\frac{\Delta f}{f} = \frac{1}{4U} \int_{\Delta V} \left(\varepsilon_0 E^2 - \mu_0 H^2\right) dV \quad , \tag{II.5.29}$$

where U is the stored energy inside the cavity

$$U = \frac{1}{4} \int_{V} \left(\varepsilon_0 E^2 + \mu_0 H^2\right) dV \quad . \tag{II.5.30}$$

So as seen in Fig. II.5.48, it is like an accordion (again) but in a different mechanical mode. This type of accordion-style frequency tuning had been also proposed around 1980 for the NC SPS single

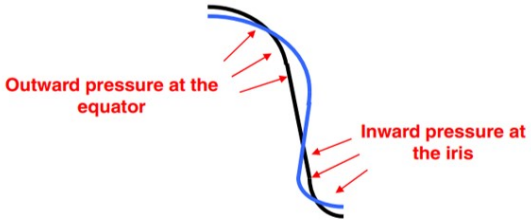

Fig. II.5.46: Deforming the cavity with EM forces.

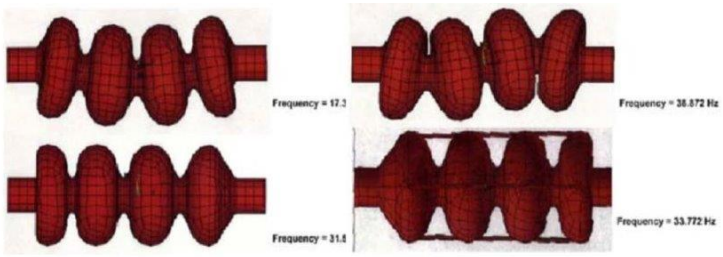

Fig. II.5.47: Mechanical oscillation modes of the cavity.

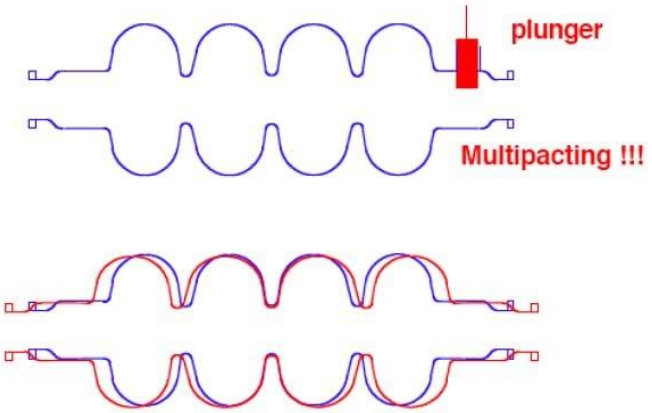

Fig. II.5.48: Compensation of cavity mode related detuning with a mechanical tuner.

cavities by some hydraulic mechanism in the tunnel but of course, never realized this way instead we had a plunging tuner (every 10 s or so) with lots of vacuum problems on its bellows.

7.6 Mechanical oscillations issues: the LEP solution

The cavity makes accordion-like movements, and the SC part must be well shielded from the fringe field of the magnetostrictive elements.

In Fig. II.5.49, a sketch for a different cavity tuner drawn by the late Joachim Tuckmantel. Thus in memoriam to Joachim, to the late Herbert Lengeler, who was one of the pioneers of SRF at CERN (see Fig. II.5.50), and to the late Philippe Bernard, who led the CERN RF group in the implementation

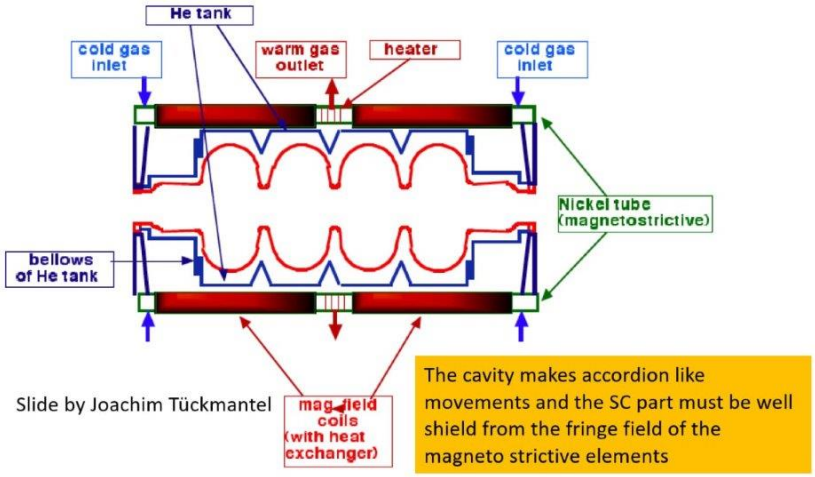

Fig. II.5.49: An alternative implementation of cavity tuner using magnetostrictive elements (drawing by the late Joachim Tückmantel).

of SRF in the LEP II collider.

Quiz: how does a magnetostrictive actuator work? Can you give an example of the magnetostrictive effect in everyday life? Hint: the humming of a transformer.

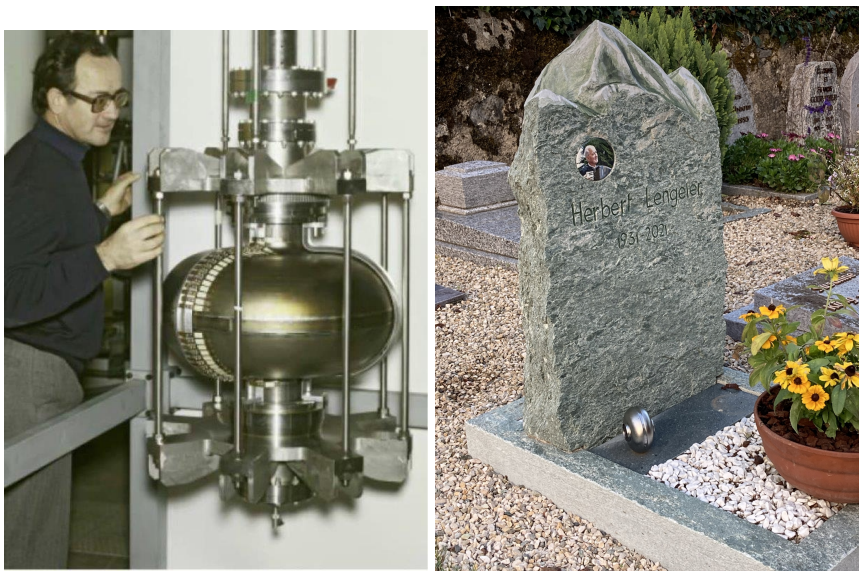

Fig. II.5.50: Herbert Lengeler, one of the fathers of SC cavities at CERN [33]. His love of SRF is manifest even on his grave.

7.7 Learning targets and quiz

After having worked through this section it would be nice if you could:

- Have an idea about SC multiple-cell resonators and their mechanical implementation;
- Know that for coupled resonators the resonance frequencies are splitting up;

- Have understood the concept of the test setup for the amplitude-dependent Q measurement on a SC cavity in particular proper control of all parameters;
- Know that the Q value of superconducting cavities is field strength dependent (Q-slope);
- Be able to give some examples of typical shapes for SC cavities;
- Be familiar with the G factor and have an idea about its order of magnitude;
- Know that the G factor gets worse for low beta cavities and why;
- Be able to explain the difference between R/Q, Q and G factor;
- Be able to draw a sketch of a 0 mode and π mode in a multiple-cell cavity;
- Know why elliptically-shaped cavities have advantages, even when they are mechanically more delicate.

7.8 Summary for the previous sections

- A lumped network circuit diagram allows an analytical description of the interaction of the RF cavity with the beam.
- The cavity is designed to minimize the reflected RF power (which would be wasted anyhow in a load) by eliminating the "reactive beam loading" through tuning the frequency of the cavity and by matching the external Q to the nominal beam current.
- Frequency tuners are in addition needed to damp frequency shifts from mechanical resonances excited by external noise sources (microphonics) or the interaction of the electromagnetic pressure with the cavity wall (Lorentz force detuning).
- Discussed in the appendix: the beam consists of bunches passing the cavity in batches of milliseconds that may excite higher order modes (HOMs) of the cavity to high voltages, if not sufficiently damped by HOM couplers.

8 Special diagnostics

8.1 Heat probes for temperature mapping on cavities 40 years ago

Many features of the cavity can be tested by RF measurements. But losses that occur in the form of localized heat can only be detected by additional diagnostics. The classical approach is temperature mapping (in the old days).

8.2 Temperature distribution measurements on SC cavity

A temperature mapping equipment from $\sim$ 1980 is shown in Fig. II.5.51. The temperature-sensing elements were Allen Bradley carbon resistors of nominally $100\,\Omega$ at ambient. The entire setup is later submerged in liquid helium. Special care had to be taken for the selection of the integrated circuit elements since normal silicon bipolar transistors "freeze" out at cryo.

Note that the measurement is not trivial, one has to properly sense the cavity wall, and not the surrounding liquid helium... There are lots of temperature probes with cryo-compatible electronics. Something which however was not trivial in the 70ies and 80ies. Can you guess why?

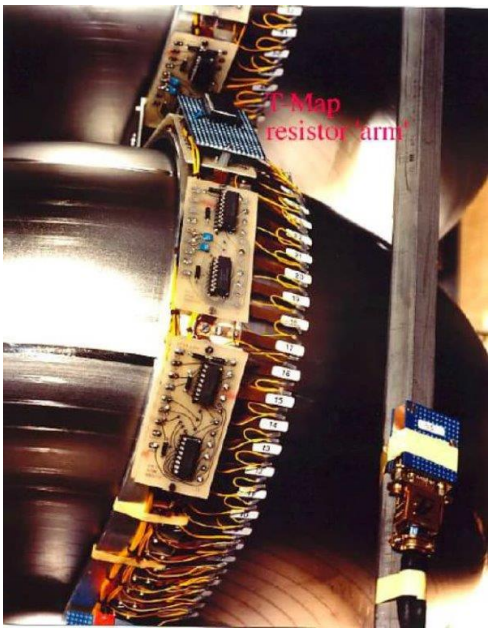

Fig. II.5.51: Temperature mapping technology in the 80ies (photo courtesy of CERN).

8.2.1 Finding hot spots

Temperature mapping is meant to localize defects. As observed in Fig. II.5.52, a hot spot was detected and later the criminal item (copper particle) was removed.

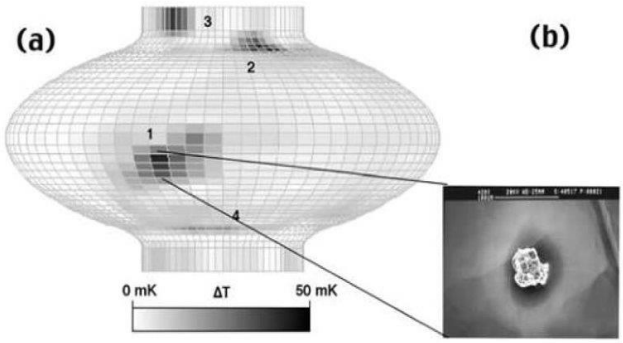

Fig. II.5.52: Hot spot from a defect found by temperature mapping [16].

8.2.2 Anomalous losses via T-mapping

T-mapping for the diagnosis of anomalous losses. In Fig. II.5.53 we see a kind of usual 2D projection that mimics the external surface of a cavity.

8.3 An introduction to the "oscillatory superleak transducer" (OST)

The second sound wave is related to the normal fluid fraction of the helium that interacts with a nanoporous membrane (pore size $< 200\,\mathrm{nm}$) while the superfluid part does not interact and passes through

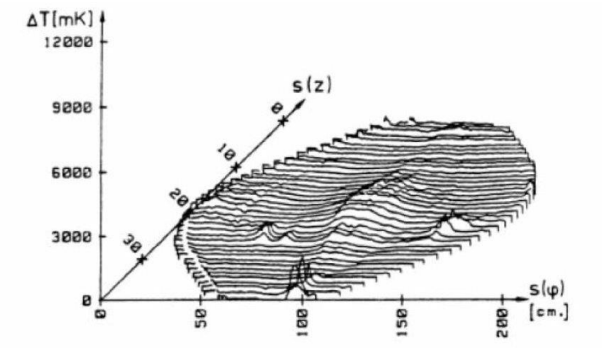

Fig. II.5.53: A temperature map in planar projection.

the pores, its coherence length being much smaller than the pore size. It was first used by K. Shepard at ANL for detecting the quench locations in SC resonators and split ring resonators and later used also for other structures [34, 35] (see Fig. II.5.54).

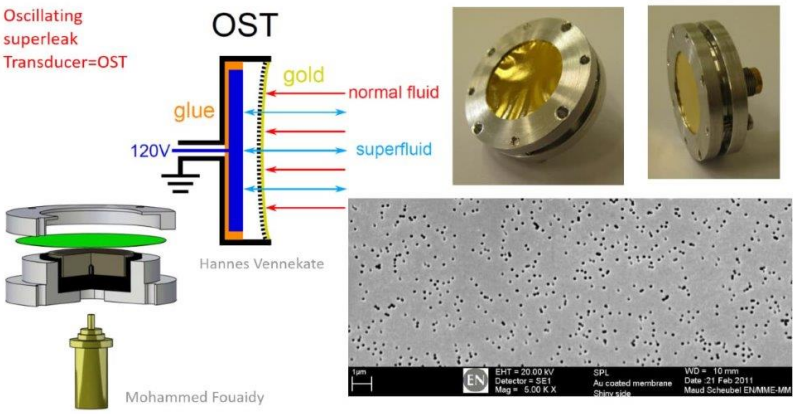

Fig. II.5.54: Second sound with superfluid helium [34, 35].

Where does the name second sound come from? The first sound wave propagates as an entropy (temperature) wave and the second is a density wave; second sound wave has a velocity of about $20\,\mathrm{m/s}$, which is really slow compared to the first sound which has a speed ten times larger. And remember the second sound wave moves the membrane since related to the normal fluid part of the He, and combined with the low speed results in a very neat way for triangulating the origin of the wave.

8.3.1 Second sound concept sound via triangulation

A quench, a thermo-magnetic breakdown of the cavity surface transitioning to the normal state, creates a sudden heat wave due to the instantaneous local increase of dissipated power. Detection and localization of quenches on superconducting RF cavities by the measurement of the second sound can be done with OSTs. The localisation of a quench can be done with a relatively small number of sensors.

A very nice triangulation method for in situ diagnostics is shown in Fig. II.5.55, where also a typical OST signal is shown.

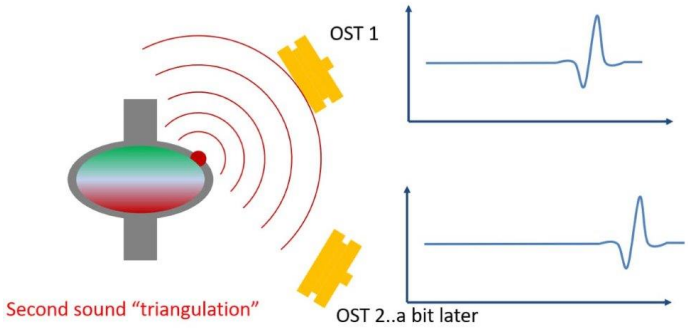

Fig. II.5.55: Second sound and quench detection via triangulation (left), and typical OST signals (right).

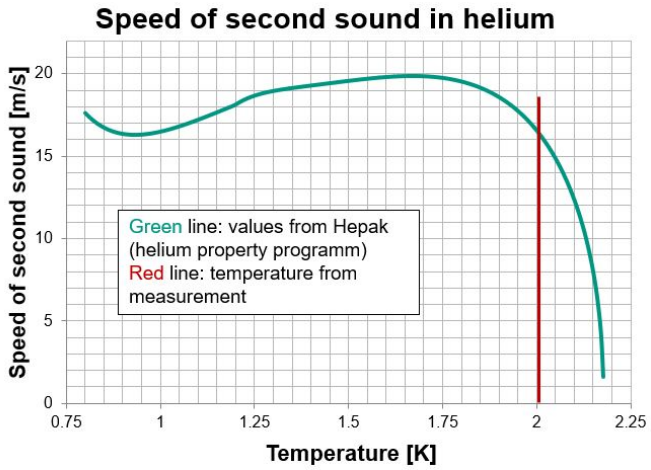

Fig. II.5.56: Velocity of second sound vs. temperature.

The measurement from Fig. II.5.56 was done at $1.977\,\mathrm{K}$ with the velocity being $v_2(1.977\,\mathrm{K}) = 17.14\,\mathrm{m/s}$. The signal of the measurement is at $2.52\,\mathrm{ms}$. Therefore, the distance to the heat source is $v_2 t = 4.32\,\mathrm{cm}$.

9 Fabrication technology

SRF cavities come nowadays essentially in two families: bulk niobium or niobium thin films coated on copper substrates. Fabrication processes, operational requirements and challenges are obviously different, but the main recurring requirements are similar:

- Maximizing the quality factor Q_0;
- Reaching high accelerating gradients E_{acc}.

However, it turns out that while maximizing Q_0 is beneficial in any given operation condition since it leads to energy savings, reaching high accelerating gradients is necessary mostly for linear accelerators which may want to maximise the energy within a given real estate. In the case of circular colliders in fact there is an optimum accelerating field which is sometimes rather low. See for example Fig. II.5.57 where the optimum working point for the CERN Future Circular Collider is studied.

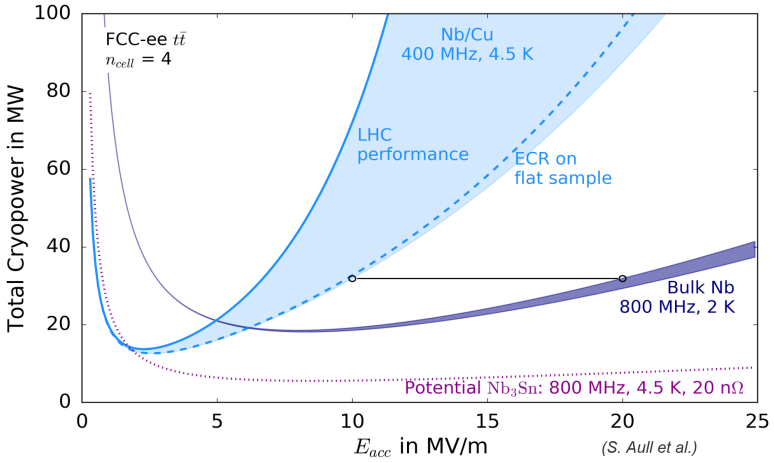

Fig. II.5.57: Optimization of the SRF system working point for the FCC-ee study at CERN [36].

How can this be? As an exercise, consider that in a circular collider, the RF system has to provide a given voltage V_{acc} per turn. The power loss is proportional to E_{acc}^2 and thus inversely proportional to the square of the length d of the accelerating system (remember, $E_{\text{acc}} = V_{\text{acc}}/d$), thus lower accelerating field E_{acc} and longer length is favored. However, the static cryogenic losses increase linearly with length. Thus we can get an optimum configuration.

Nevertheless, even in a circular collider, the field requirement presents challenges for the fabrication processes and the technological requirements. Most of these are related to residual or extrinsic losses of the cavities.

9.1 Anomalous losses

The so-called "anomalous losses" account for all contributions to the RF losses that are not described by the intrinsic parameters of the superconducting material (critical temperature, critical field, BCS (or two fluid) surface resistance R_s, etc). These anomalous losses show up as heat and are visible in the $R_s(T)$ and $Q_0(E_a)$ plots, as well as in the "temperature maps". These are often well characterized during RF measurements like in Fig. II.5.58 where several anomalous loss mechanisms are shown. We describe now some of the various anomalous losses as illustrated in the figure. All this is discussed in great detail in the book [37].

9.1.1 Residual losses

Typical residual losses are due to extrinsic defects in the superconducting material: localized impurities (Ta inclusions, projections from welds), defects (welding seams, scratches), excess hydrogen that segregates at low temperature in highly dissipating niobium hydrides, trapped ambient magnetic field. For example, cavities undergo typically hydrogen outgassing at high temperatures (see Fig. II.5.59) to remove hydrogen and prevent the so-called H-disease, that is the segregation of hydrides.

For classical superconductors do make sure that there is no trapped magnetic flux during cool-down! Trapped fluxons (the quanta of magnetic flux in which the field is divided in type-II supercon-

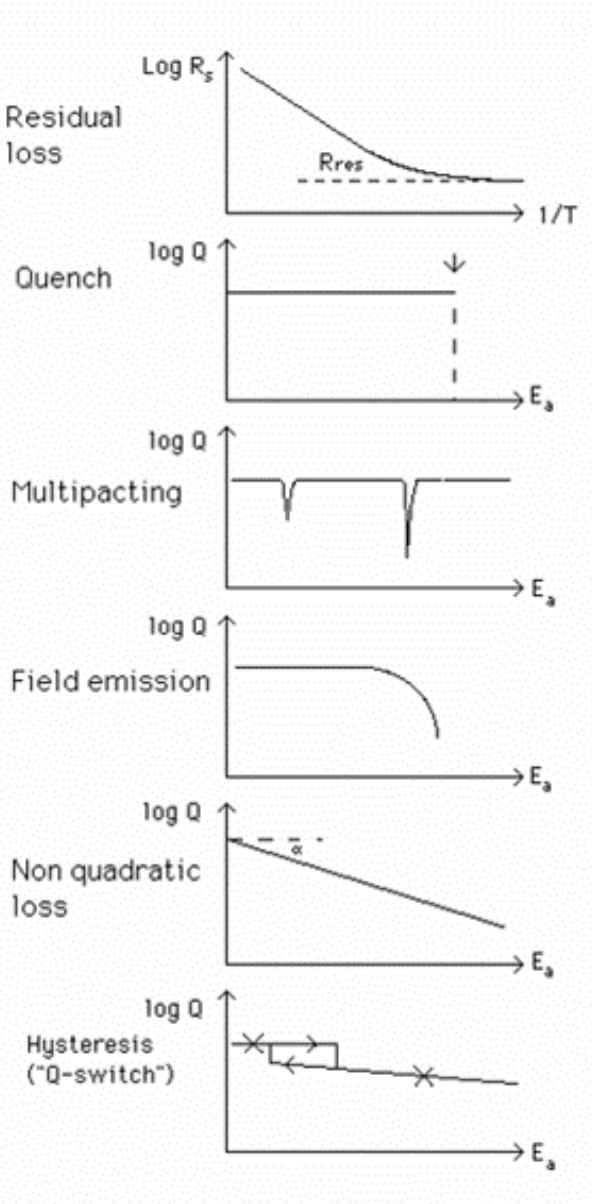

Fig. II.5.58: Different anomalous loss mechanisms [38].

ductors) oscillate under the Lorentz force induced by the RF surface currents and dissipate energy, like in a harmonic oscillator where dissipation is due to viscous dissipative term. The larger the conductivity (normal state, in the vortex core), the larger the dissipation. Bulk niobium cavities suffer orders of magnitude more than thin film cavities, which have lower purity. So we may have accelerators without shielding, like LEP and the LHC, with Nb-coated cavities! In accelerators with Nb-bulk cavities one needs shielding, but one can also play tricks with very fast cooling to reduce the amount of trapped flux (see Fig. II.5.60).

High T_c superconductors can work nicely in a strong static magnetic field e.g. applied for axion search cavities but their Q value is significantly lower than for classical RF superconductors.

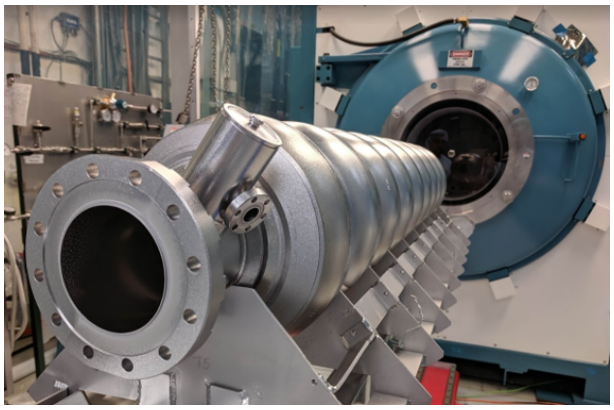

Fig. II.5.59: Typical UHV high-temperature furnace for hydrogen outgassing [39].

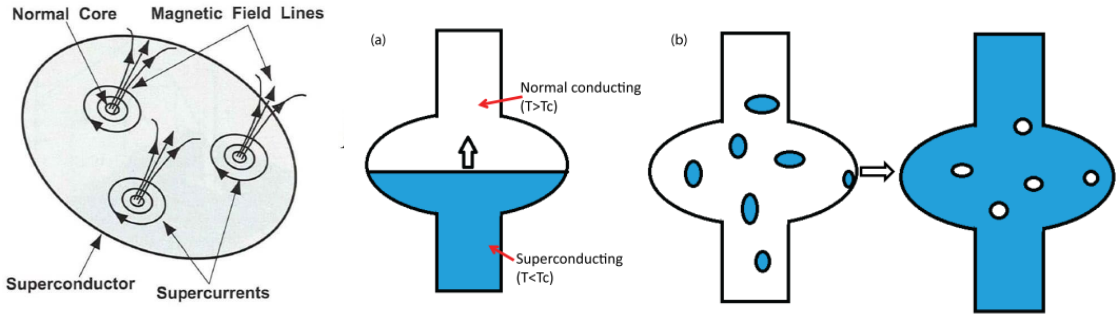

Fig. II.5.60: Trapped magnetic flux [12], and how a fast cool down expels all the magnetic field; slow cool down allows the field to be trapped at some isolated locations [40].

9.1.2 Quenches

A quench is also called thermo-magnetic breakdown. What happens? Imagine having a defect, for example, a normal conducting inclusion. This will dissipate power more than the surrounding niobium. As the field increases it will reach soon a temperature larger than T_c (heating the surrounding Nb above T_c too) leading to a chain reaction and bringing all cavity surfaces to the normal state. The main driver for suppressing quenches, apart from eliminating defects as will be discussed later, is to improve the thermal conductivity of niobium so as to better evacuate any extra heat. This is shown in Fig. II.5.61. When electrons are paired in Cooper pairs in a superconductor they are no longer "available" for heat transfer. The only electrons available are the non-paired ones, and to optimize their heat-transfer capabilities it is important to minimize their scattering with impurities. Purification of niobium was in the past the main technological development required by SRF to fabricate useful cavities.

The RRR is a key parameter for heat conductivity, industrial-grade Nb has a RRR of 40, while the requirements of SRF have driven the manufacturers to produce industrially Nb with an RRR of 300 and more. This can easily be purchased nowadays (but has a cost similar to silver!). Remember even if RRR is high, only a fraction of electrons contributes to thermal conductivity!

This is different compared to copper: copper is the best conductor (forgetting silver...), it is rather cheap and it can be obtained in high purity, with very high RRR, and now all electrons conduce heat! A

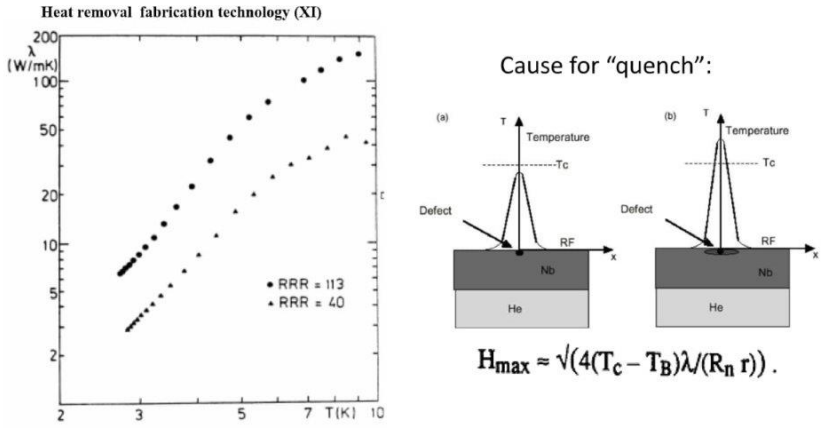

Fig. II.5.61: Thermal improvement of thermal conductivity for Niobium sheets.

neat technological solution is then to make cavities of copper body, coated with a thin film of niobium. This technology was developed at CERN for LEP. It totally prevents quenches, and adds several benefits: it is much cheaper and is particularly relevant for large cavities of low frequency, and allows eliminating magnetic shielding. But there are also disadvantages, discussed later.

Coatings are usually done by sputtering, but the novel trend is to move to the High-power impulse magnetron sputtering (HiPIMS) technology: sputter coatings are obtained by neutral Nb atoms, while in HiPIMS Nb is ionized and directed to the surface at higher energy. For an illustration of a sputtering system, see Fig. II.5.62.

9.1.3 Electron field emission

We have already discussed the effect of electron multipacting, which happens at low field (requires the electron energy < few keV to have secondary SEY > 1). The same principle of electron field emission may cause troubles at high fields too. The nasty consequence of (hidden) electron field emission emitters can be seen in Fig. II.5.63.

Electrons are field-emitted and impact the cavity surface, bringing two possible consequences if the electron current is large enough: at large E_{acc} field they absorb energy stored in the cavity, thus lowering the quality factor Q_0. And if the acquired energy is large enough, the electron might even heat up the location where they impinge, leading possibly in some cases (in particular in bulk-Nb which has poor thermal conductivity) to a quench!

At the origin of field emission, we must have of course some localized field emitters. Typical particulate emitters containing impurities are shown in Fig. II.5.64.

The electron current produced by field emitters is due to the quantum tunneling effect: the externally applied field lowers the energy surface barrier (the work function Φ) thus tunneling becomes more probable, actually increasing exponentially with the applied field. This is the so-called Fowler-Nordheim tunneling. The principles of Fowler Nordheim theory are shown in Fig. II.5.65.

The only practical way to prevent field emission is to have the best possible surface cleanliness: avoid particles, defects, etc. Therefore, clean room preparation is mandatory as shown in Fig. II.5.66.

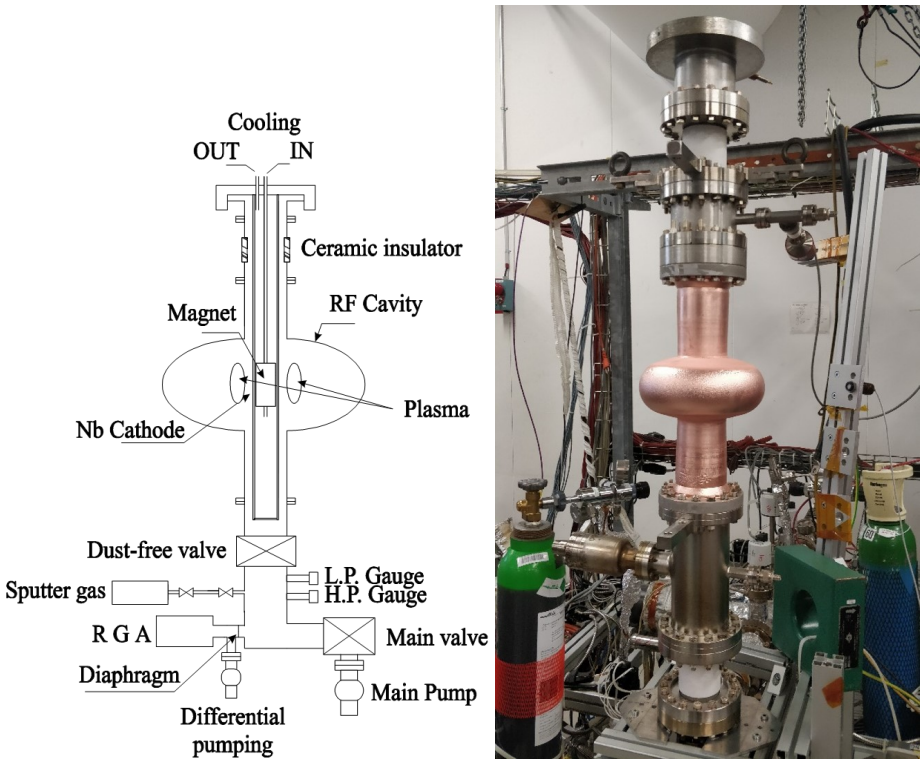

Fig. II.5.62: Left: Schematics of a typical Nb/Cu sputtering system [41]. Right: How it looks in reality with a 1.3 GHz prototype cavity being coated [42].

All SRF cavity assembly procedures are done in a microelectronics-like environment: clean rooms are ISO5 - Class 100 type, with localized cleanliness levels up to ISO4 - Class 10. This allows to avoid any possible surface contamination. But how to clean surfaces, to start with?

The best way to clean a surface and remove particulate contamination is high-pressure water rinsing (HPWR). This is done with demineralized water, effectively free of any soluted element or contaminants (resistivity $18\,\mathrm{M\Omega\,m}$ and filtered with nanoporous filters $< 100\,\mathrm{nm}$), performed at pressures in excess of $100\,\mathrm{bar}$ with very high water flows ($1\,\mathrm{m^3/h}$), for duration of several hours and inside a clean room. The cavity is sprayed with water and then dried inside the clean room, so no more particles will contaminate the surface (Fig. II.5.67).

Many details of clean room work have already been discussed elsewhere. It is just important to remember that without proper clean-room facilities, the reliable industrial production of superconducting cavities becomes very questionable and inefficient.

9.1.4 Electropolishing

The requirements for high-quality surface preparation don't stop here. In order for particles not to "stick" and to facilitate removal, a high surface smoothness is required. It turns out that surface smoothness is needed also for obtaining the lowest possible residual surface resistance. So referring to Fig. II.5.58, electropolishing helps with residual losses, field emission, and also non-quadratic losses that we'll discuss later.

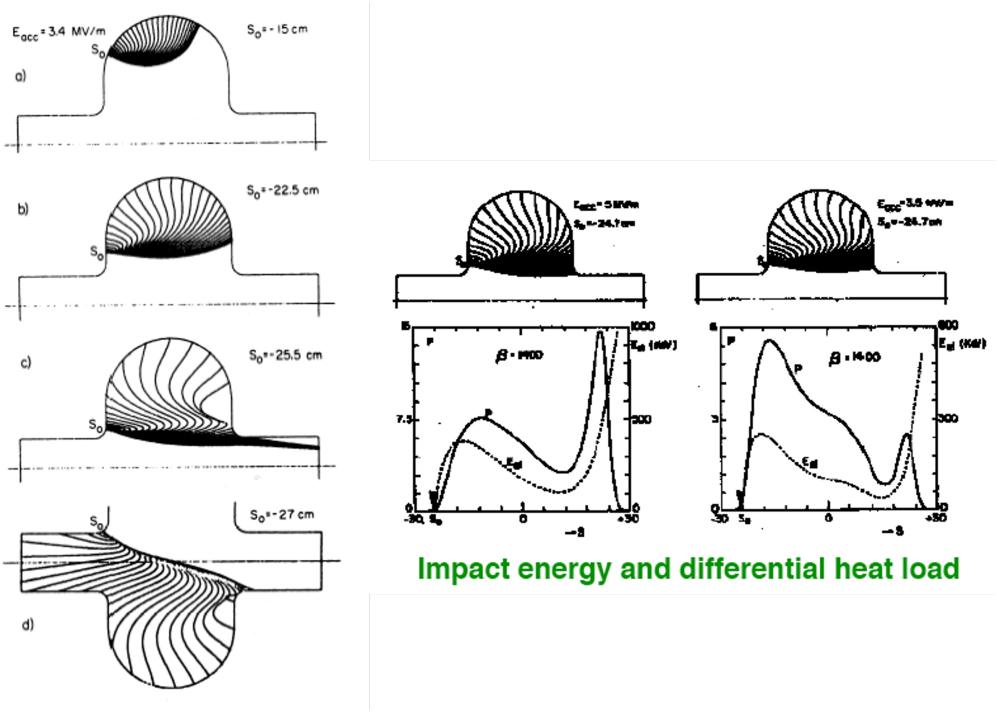

Fig. II.5.63: Diagnostic field emission [43].

In electropolishing the metal is immersed in an electrolyte as shown in Fig. II.5.68, and subjected to direct current. The metal part to be treated is made anodic and under certain conditions, a controlled dissolution of the metal is achieved. The electrolyte is chosen to have a high viscosity, thus metal high migration is diffusion-limited. In such cases, the protruding tips are removed faster than the valleys, and this results in a smoothing effect. This process allows for the best results for SRF cavities. Mechanical polishing may give the best apparent roughness, but results in a damaged surface layer which is very detrimental for cavity performance. Chemical polishing (high-viscous solution of strong acids) results in smoothing too, but leaves grain boundaries exposed, which enhances the local magnetic field and promotes early transition. Electropolishing guarantees the best compromise: the metal is left in its most pristine state, low-wavelength roughness is minimized, and high-wavelength roughness (compared to the skin depth) is not relevant for SRF performance. The different effects from different techniques are shown in Fig. II.5.69.

9.1.5 Non-quadratic losses

Putting all the above together following the path shown in Fig. II.5.70 results in state-of-the art cavity performance, and some very good results on 1.3 GHz TESLA-shape cavities are shown in Fig. II.5.71. However, some losses still remain, sometimes called non-quadratic losses. These are the type of anomalous losses of more difficult interpretation and minimization. Assuming the surface resistance is field-independent (equivalent to saying that Q_0 is field independent), power dissipation theoretically should go with surface fields squared (hence quadratic). Any field dependence of the surface resistance results in more-than-quadratic losses (hence non-quadratic), or in a Q_0 decrease with field (called “slope” in

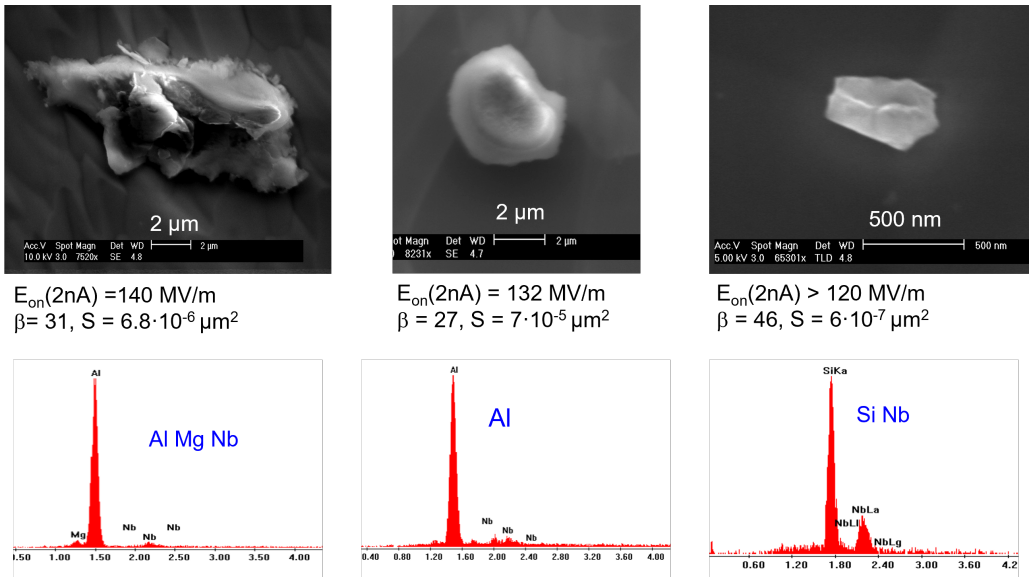

Fig. II.5.64: Electron field emitters of different sizes and nature; the characteristic composition is indicated in the graphs in the lower row [14].

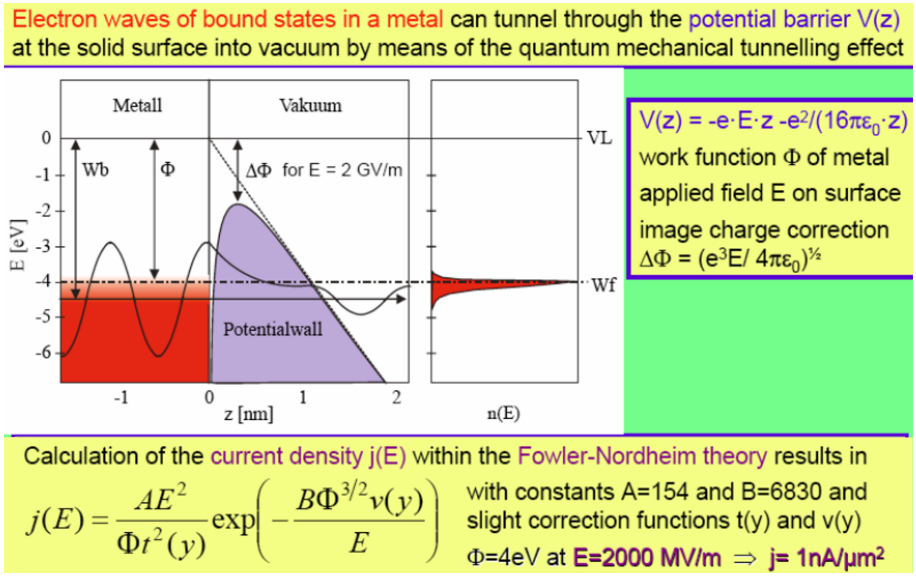

Fig. II.5.65: The mechanism of field emissions from flat metal surfaces [44].

SRF jargon), as illustrated in the Q_0 vs. E_{acc} of Fig. II.5.72.

Many mechanisms might be responsible: intrinsic nonlinear mechanisms, extrinsic effects of impurities, RF flux penetration and hysteresis, and thermal feedback (the surface heats up due to poor cooling).

The case of Nb/Cu cavities is interesting: it appears that their slope is much larger than for Nb bulk. This has plagued Nb/Cu cavities since their inception, and no reasonable explanation has been found to date. Clearly, it is not due to thermal feedback, the conductivity of copper being so large! It might be due to a thermal exchange limitation at the Nb/Cu interface, or perhaps to micro-quenches

Fig. II.5.66: Clean room preparation on one of the superconducting cavities for the LEP-2 upgrade [45].

Fig. II.5.67: Demonstrating HPWR in a test transparent plastic cavity [46].

due to local delamination of the film. A major delamination of the film results in a major Q-switch: increasing the field in a cavity induces a small region of poor contact with the substrate to turn normal; when decreasing the field, it remains normal conducting thus highly dissipating until the field level is very small (this is the last case of Fig. II.5.58). Imagine now a sequence of many micro-Q-switches, individually invisible. This could mimic the Q-slope in Nb/Cu cavities. Actually, this is what has motivated the use of HiPIMS coating technology. HiPIMS improves adhesion thanks to the Nb-ion energy and eliminates micro-defects and parasites in Nb/Cu films, see Fig. II.5.73. The first results, yet unpublished, indicate that this is the way to go: recent LHC-type cavities are almost slope-free! It remains that Nb/Cu cavities have usually a level of impurities dissolved in the Nb which is higher than for bulk. This results in a BCS surface resistance which is improved compared to bulk Nb, see Fig. II.5.7, allowing a better performance at $4.2\,\mathrm{K}$. This impurity level is also responsible for the lower sensitivity to external magnetic field compared to bulk, as mentioned earlier. But it has no impact (and perhaps a negative one?) on the performance at $1.9\,\mathrm{K}$, where the BCS surface resistance has vanished.

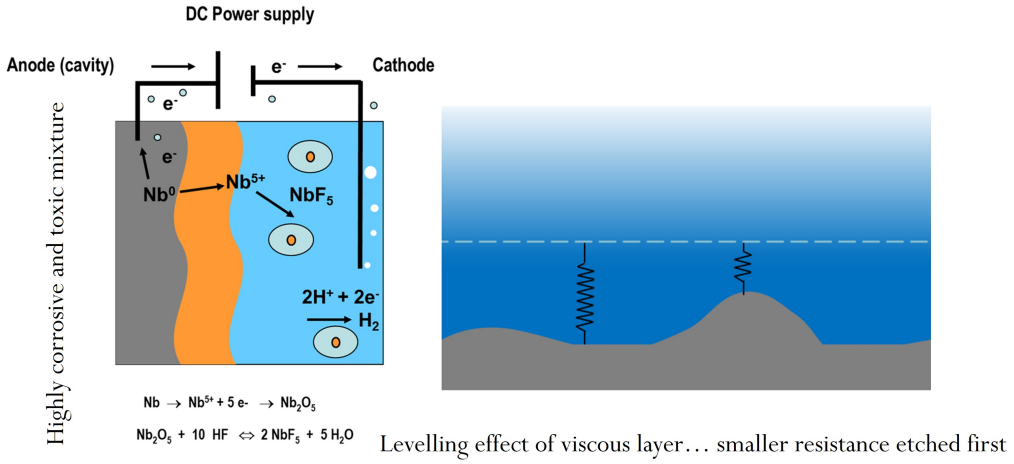

Fig. II.5.68: Electopolishing technology (Image courtesy of C. Antoine).

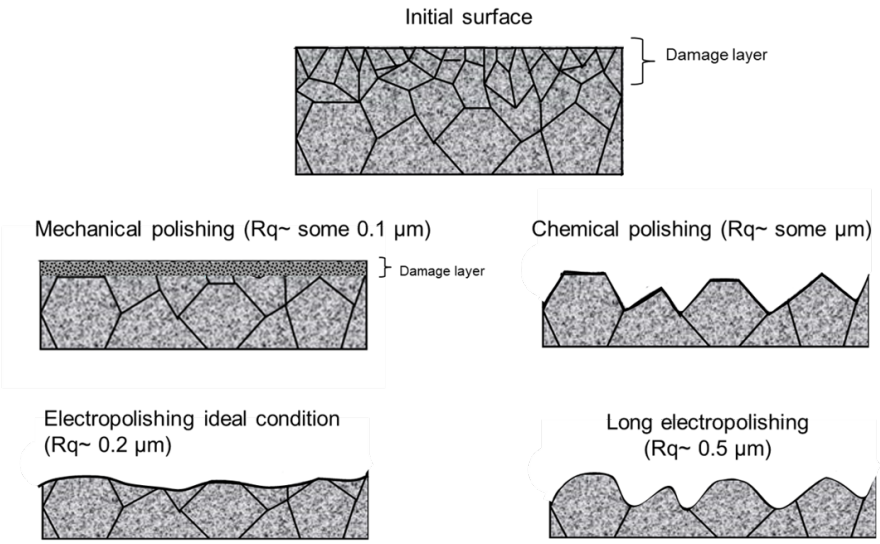

Fig. II.5.69: Illustration of the effects of different polishing procedures (Image courtesy of C. Antoine).

However, the perhaps most surprising recent discovery is the anti-Q-slope! This has been identified at Fermilab and is illustrated in Fig. II.5.74. This happens when the bulk Nb is "doped" with a specific and small amount of impurities, typically nitrogen. The slope has a positive coefficient, and this is due (and has been proven and validated theoretically) to some subtle effects related to non-equilibrium quasi-particle states in the BCS gap: as you see SRF has deep theoretical implications, and this matter will not be discussed here further.

9.2 Stochastic parameters

All the discussion above is neatly summarised in the following Table II.5.4.

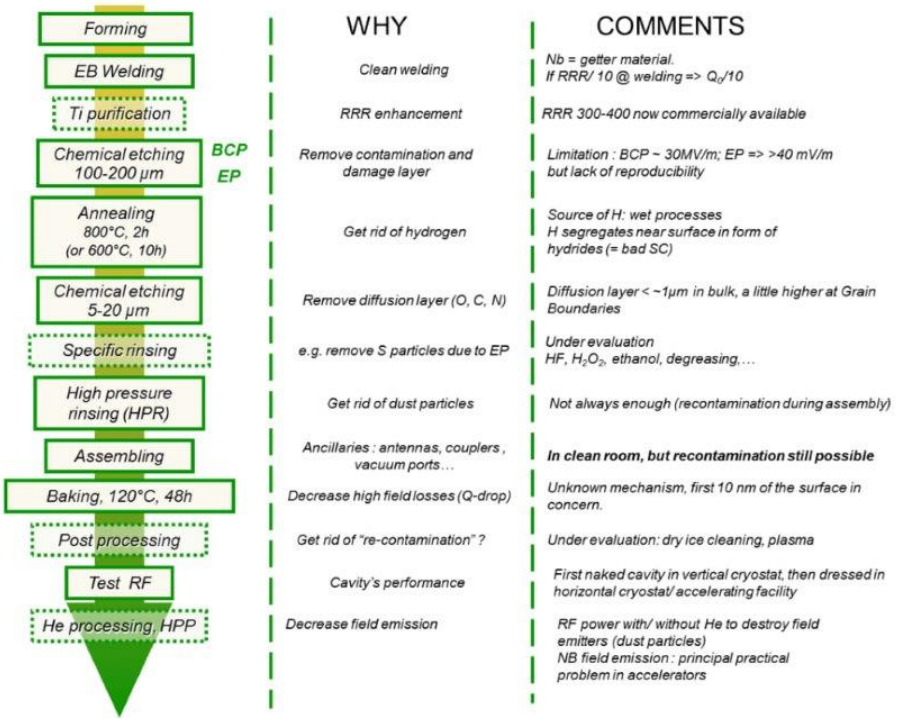

Fig. II.5.70: Combined effects of surface preparation improvements: EP, HPWR, etc. [47].

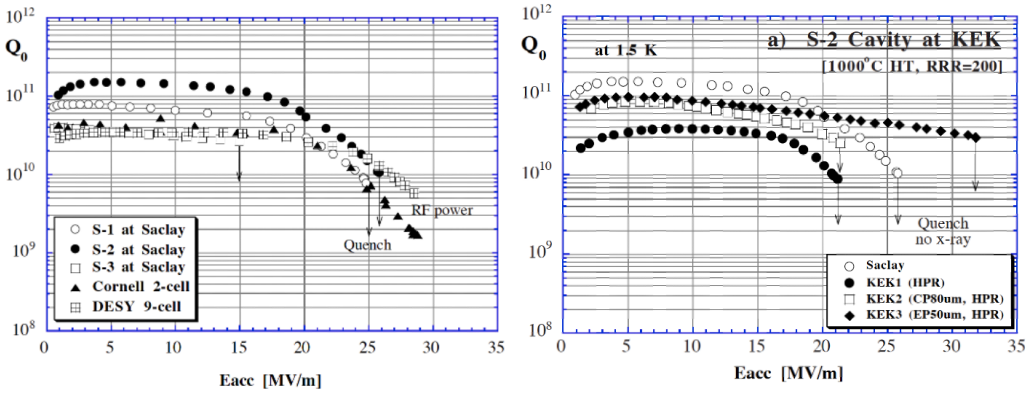

Fig. II.5.71: Test results at Saclay, Cornell, and DESY (left) and the S-2 cavity at KEK (right) [48].

9.3 State of the art SRF research

Reaching ultimate performance with bulk Nb cavities or Nb/Cu thin film cavities is the aim of current R&D in the field of SRF. Several challenges however are already defined at the forefront of the current activities, beyond niobium-based cavities:

- Low-temperature superconductors: Nb-based and alternative materials;
- High-temperature superconductors.

In the search of new materials beyond Nb (i.e. Nb_3Sn, V_3Si, NbN for low temperatures and YBCO for high temp) the primary goal is energy saving, not so much the absolute performance in terms

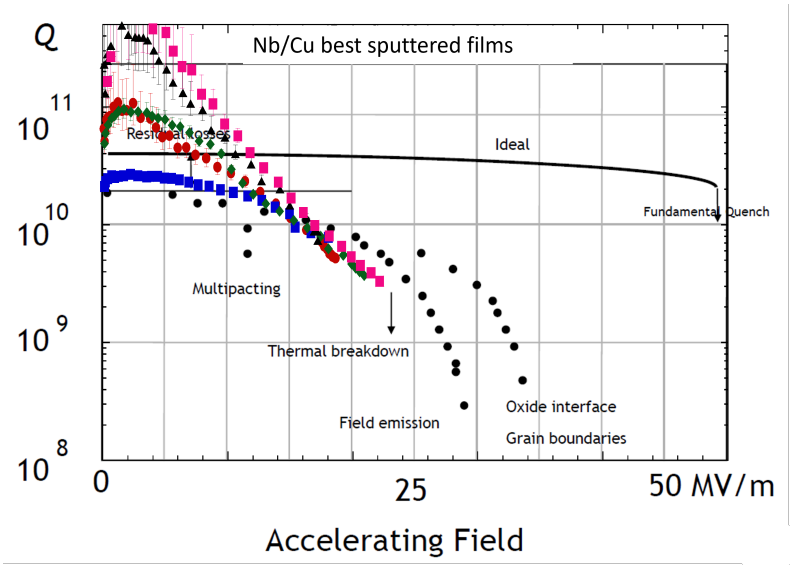

Fig. II.5.72: "Slope" of different types of cavities compared to the ideal case which has practically flat curve, except when surface current density approaches critical current density.

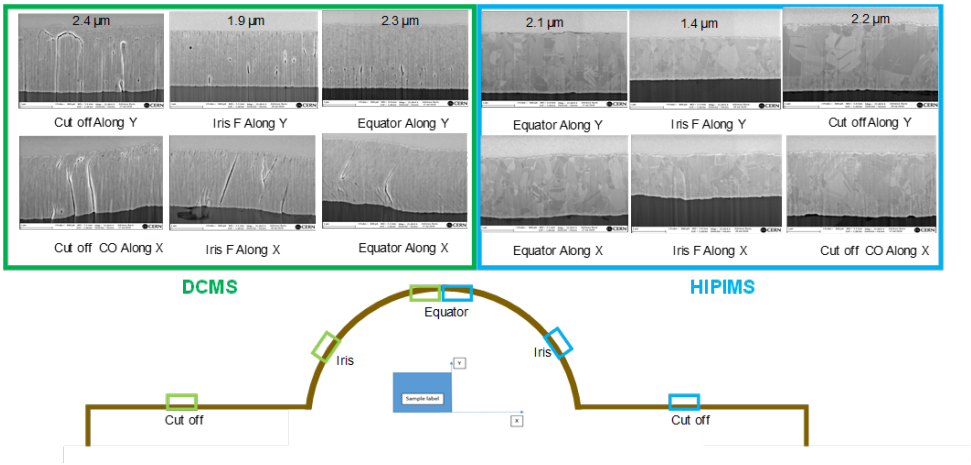

Fig. II.5.73: Film structure of conventional sputter-coated Nb films, compared to the film deposited by HiPIMS (Image courtesy of G. Rosaz).

of accelerating gradient. Remembering Fig. II.5.9, one would ideally look for materials that have R_{BCS} at their operating temperature as small as that of Nb at $1.9\,\mathrm{K}$, while still maintaining a very low residual resistance. If such goal could be attained, this would open up potential very large energy savings. For example, if operation at $4.5\,\mathrm{K}$ would be possible, this would result in a saving of a factor of about three compared to operation at $1.9\,\mathrm{K}$, and even larger if higher temperatures could be used, as discussed at the beginning of this lecture. Of course, the same other operational performance and reliability of existing cavities should be guaranteed.

A potential first application of novel materials may come from the use of Nb_3Sn. This material is actively being researched following different paths for realization, either by Sn diffusion into Nb bulk cavities [49] or by sputtering of a Nb_3Sn thin film onto Cu cavities [50]. Excellent results have recently

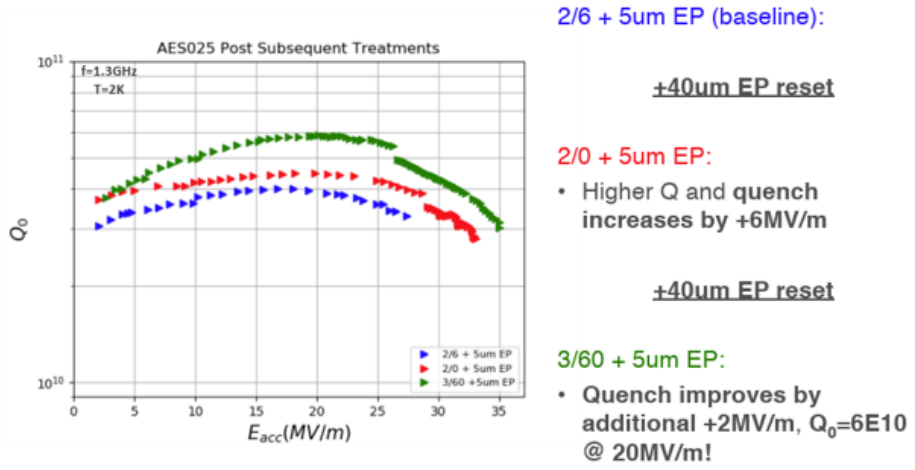

Fig. II.5.74: "Slope" of cavities with different types of nitrogen doping (Image courtesy of A. Grassellino).

being obtained, and the technique of Sn diffusion has a long pluri-decennial story behind it and is mature enough so that some cavities have been produced. A first application, and a reason why the technology is actively pursued, could be in future high-energy circular colliders, where as explained in Fig. II.5.57 the goal is to look for optimal Q_0 at a rather low, optimal accelerating field.

Work on higher-critical-temperature materials such as YBCO has only recently started, following recent development in material fabrication. Future history will tell whether these material would allow working at even higher temperatures, opening up major energy savings for future-generation accelerators.

9.4 Summary

- The choice of the technology (normal conducting vs. superconducting) depends on various parameters: mass of the accelerated particle, beam energy, beam current, mains power consumption, etc.
- If superconducting, the typical interval of RF frequencies is between 300 MHz and 3 GHz.
- The technically most suitable superconducting material is niobium, choosing lower frequencies allows operation at 4.2 K to 4.5 K, the boiling temperature of ℓHe, higher frequencies request operation at 1.8 K to 2 K. However, the cryogenic installation is much more demanding.
- The production of SC cavities requests careful application of quality control measures during the whole cycle of assembly to avoid performance degradation by "anomalous losses".
- The "anomalous losses" contribute to an extra heat load, which is expensive to cool and may limit the performance.

10 Conclusion

We have tried to give an overview of the state of the art of SC RF technology including a short recap on theory, history, and motivation for the application of this technology. One important part is the diagnos-

Table II.5.4: A summary of all stochastic and extrinsic causes of anomalous losses

Influencing quantity	**Impact quantity**	**Physical explanation**	**cure**
Field emission sites (foreign particles sticking to the surface, size, density)	Q-value / acc. gradient γ radiation HOM coupler quench	Modified Fowler-Nordheim-theory	Assembling in dust-free air, rinsing with ultra-pure water (control of resistivity and particulate content, of outlet water) and alcohol, high-pressure ultra-pure water rinsing (ditto), "He- processing", heat treatment at $800\,^{\circ}\mathrm{C}$ to $1400\,^{\circ}\mathrm{C}$, electro-polishing (indirect effect)
Secondary emission coefficient δ	Electron-multipacting	Theory of secondary electron emission	rounded shape of cavity, rinsing with ultra-pure water, bake-out, RF - Processing
Unknown	Q – slope / Q-drop (Q – value / acc. gradient)	Unknown (early field penetration in hydride highly suspected)	Annealing $150\,^{\circ}\mathrm{C}$, Electro-polishing
Metallic normal-conducting inclusions in Nb	Acc. gradient	Local heating up till critical temperature of Nb	Inspection of Nb sheets (eddy current or SQUID scanning), removal of defects ($\approx 1\,\mu\mathrm{m}$), sufficiently large thermal conductivity ($30\,\mathrm{W/mK}$ to $40\,\mathrm{W/mK}$) cleanliness of tooling for manufacturing and handling
Residual surface resistance	Q-value / acc. gradient	Unknown to a large extent	Quality assurance control of a multitude of parameters

tics and measurement of RF superconductors as samples and in situ. Different shapes of SC cavities are discussed including historical aspects of the evolution of presently used cavity implementations. Practical issues mentioned include surface reliable surface preparation to minimize electron emission and multipactor. Many examples of present-day applications are shown and also compared. The present paper/article can only serve as an introduction and short overview of the amazing and exciting field of RF superconducting technology.

Acknowledgements

The authors would like to thank in particular Wolfgang Weingarten who is the grandfather of this lecture (more than 20 years ago) which underwent many modifications and hopefully improvements over the years. Manfred Wendt made important contributions in constructive criticism, as well as simplifications. Sarah Aull and Tobias Junginger made many contributions to earlier versions of these lectures. A lot of material was contributed by Eric Montesinos. We owe a big thanks to Marios Maroudas for large contributions to the editing work and Jens Vigen for support, help, and encouragement. Claire Antoine for important comments, contributions, and clarifications. Finally, this paper would not have been possible in this version without the permanent support and help from JUAS and also from CERN.

Appendices

II.5.A Complex conductivity, London equations

The two-fluids model stipulates that a superconductor has two populations of current carriers:

- "normal conducting" electrons have the usual resistive behavior;
- "superconducting" electrons have only an inductive response.

In parallel, they contribute to electrical conductivity and surface resistance. The surface resistance goes to zero at 0 K, and takes the value of the normal-conducting metal at T_c.

We should also recall here that the London penetration depth for a superconductor is equivalent to the skin depth of a normal metal. It is orders of magnitude smaller, and frequency-independent

II.5.A.1 London equations

Here are the two London equations

$$\frac{\partial \boldsymbol{j_s}}{\partial t} = \frac{n_s e^2}{m}\boldsymbol{E} \quad , \tag{II.5.31}$$

$$\nabla \times \boldsymbol{j_s} = -\frac{n_s e^2}{m}\boldsymbol{B} \quad , \tag{II.5.32}$$

where the symbols have the usual meaning, and n_s is the density of electrons in the superconducting state.

By applying $\boldsymbol{B} = \nabla \times \boldsymbol{A}$ on the vector potential $\boldsymbol{A}$ we get

$$\boldsymbol{j}_s = -\frac{n_s e^2}{m}\boldsymbol{A} = -\Lambda^{-1}\boldsymbol{A} \quad . \tag{II.5.33}$$

We introduce this way a term Λ which is a specific inductance. This expression looks very similar to Ohm's law that stipulates as $j = \sigma E$.

By applying Ampere's law to Eq. II.5.32 we get

$$\nabla^2 \boldsymbol{B} = \frac{1}{\lambda_L^2}\boldsymbol{B} \quad , \tag{II.5.34}$$

where

$$\lambda_L = \sqrt{\frac{m}{\mu_0 n_s e^2}} \quad . \tag{II.5.35}$$

From Eq. II.5.34 we can derive the exponential decay of the B-field inside the superconductor with decay constant λ_L, known as the London penetration depth, see Fig. II.5.A.1. Typical values for λ_L in different superconductors are shown in Table II.5.A.1.

II.5.A.2 Plane waves in vacuum

From Maxwell's equations

$$E = E_0 e^{j(kz-\omega t)} \quad , \tag{II.5.36}$$

Table II.5.A.1: Compare to NC Cu skin depth: $2\,\mu\mathrm{m}$ at $1\,\mathrm{GHz}$.

Element	**Al**	**Nb (crystal)**	**Nb (film)**	**Pb**	**Sn**	**YBCO**
$\lambda_L[\mathrm{nm}]$	50	47	90	39	51	170

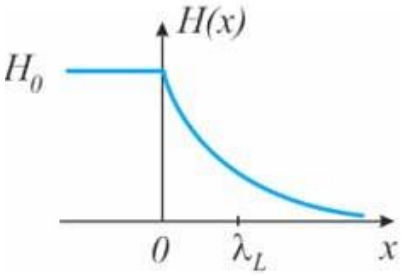

Fig. II.5.A.1: Visualisation of the London penetration depth λ_L.

$$H = H_0 e^{j(kz-\omega t)} \quad , \tag{II.5.37}$$

$$H = E_0 \frac{k}{\omega\mu_0} e^{j(kz-\omega t)} \quad , \tag{II.5.38}$$

with the wavenumber

$$k = \frac{2\pi}{\lambda} = \frac{\omega}{c} = \omega\sqrt{\varepsilon_0\mu_0} = \sqrt{\frac{\varepsilon_0}{\mu_0}} = a + j\beta \quad , \tag{II.5.39}$$

follows the wave equations in free space

$$E = E_0 e^{j(kz-\omega t)} \quad , \tag{II.5.40}$$

$$H = E_0\sqrt{\frac{\varepsilon_0}{\mu_0}} e^{j(kz-\omega t)} \quad , \tag{II.5.41}$$

with the free space impedance:

$$Z_0 = \frac{|\boldsymbol{E}|}{|\boldsymbol{H}|} = \sqrt{\frac{\mu_0}{\varepsilon_0}} = 376.7\,\Omega \quad . \tag{II.5.42}$$

II.5.A.3 Plane waves in normal conducting metals

The generalized wavenumber is given by

$$k^2 = \omega^2\varepsilon\mu + j\omega\sigma\mu \quad , \tag{II.5.43}$$

and

$$Z_0 = \frac{|\boldsymbol{E}|}{|\boldsymbol{H}|} = \sqrt{\frac{\mu}{\varepsilon}} = \frac{\omega\mu}{k} \quad , \tag{II.5.44}$$

where $\mu = \mu_0\mu_r$, $\varepsilon = \varepsilon_0\varepsilon_r$. The local current density is given by the Ohm's law $\boldsymbol{j}(x,t) = \sigma\boldsymbol{E}(x,t)$. The surface current density H has the dimension Ampere/meter. The conductivity in a normal-conducting metal is

$$\sigma(\omega) = \frac{\sigma_0}{(1 + j\omega\tau)} \quad , \tag{II.5.45}$$

with τ the relaxation time between two electron collisions and

$$\sigma_0 = \frac{ne^2\ell}{m_e v_F} = \frac{ne^2\tau}{m_e} \quad , \tag{II.5.46}$$

where m_e = is the effective electron mass, e = the elementary charge, ℓ is the electron mean free path and v_F the Fermi velocity ($\ell = \tau v_F$).

In practice, σ is assumed to be frequency independent ($\omega\tau \ll 1$) and real (below optical frequencies)

$$\omega\sigma\mu \gg \omega^2\varepsilon\mu \Rightarrow k^2 = j\omega\sigma\mu \quad . \tag{II.5.47}$$

The wave equation in metals is then given by

$$E = E_0 e^{j(kz-\omega t)} = E_0 e^{j(\alpha z-\omega t)} e^{-\beta z} \quad , \tag{II.5.48}$$

since $e^{jj\beta z} = e^{-\beta z}$ with

$$\frac{1}{a} = \sqrt{\frac{2}{\sigma\omega\mu_0}} = \delta \quad . \tag{II.5.49}$$

Caveat: $\boldsymbol{j}(x,t)$ = surface current density; $j = \sqrt{-1}$; δ = field penetration or skin depth in normal metals; σ_0 = conductivity at DC.

II.5.A.4 Definition of terms and comparison NC-SC

A comparison of the related equations between SC metal and NC metal is shown in Tab. II.5.A.2.

Table II.5.A.2: Comparison of superconductor (two-fluid model) with normal conductor [38].

Superconducting metal	**Normal-conducting metal**
$curl\boldsymbol{H} = \boldsymbol{j} + e_0\,(d/dt)\,\boldsymbol{E}$ $curl\boldsymbol{E} = -\mu_0\,(d/dt)\,\boldsymbol{H}$ $div\boldsymbol{H} = 0$ $div\boldsymbol{E} = 0$	
$(d/dt)\,\boldsymbol{j} = \boldsymbol{E}\left(\mu_0\lambda_L^2\right) + \sigma_n\,(d/dt)\,\boldsymbol{E}$ $curl\boldsymbol{H} = -\boldsymbol{H}/\lambda_L^2 - \sigma_n\mu_0\,(d/dt)\,\boldsymbol{h}H$	$\boldsymbol{j} = \sigma_n\boldsymbol{E}$
$\Delta\boldsymbol{E} = -K^2\boldsymbol{E}$ $\Delta\boldsymbol{H} = -K^2\boldsymbol{H}$	
$K^2 = -\lambda_L^2(1 - j\sigma_n\mu_0\omega\lambda_L^2 - \varepsilon_0\mu_0\omega^2\lambda_L^2)$ $Z_{S_{SC}} = (1/2)\omega^2\mu_0^2\lambda_L^3\sigma_n + j\omega\mu_0\lambda_L$ $\varepsilon_0\mu_0\omega^2\lambda_L^2 \ll \sigma_n\mu_0\omega\lambda_L^2 \ll 1$	$K^2 = \varepsilon_0\mu_0\omega^2\,[1 + j\sigma_n/\,(\omega\varepsilon_0)]$ $Z_{S_{NC}} = (\omega\mu_0\delta/2)(1+j) = \sqrt{[\omega\mu_0/\,(2\sigma_n)]}(1+j)$ $\omega\varepsilon_0/\sigma_n \ll 1$
Effective electron mass m Electron mean free path l Conductivity of the NC electrons $\sigma_n = \ln_n e^2/\,(mv_F)$ London penetration depth $\lambda_L = \sqrt{m/\,(n_s e^2\mu_0)}$	Surface impedance $Z_S = (E_z/H_y)\vert_{x=0} = \mu_0\omega/K$ skin depth $\delta = \sqrt{2/\,(\mu_0\sigma_n\omega)}$ Fermi velocity v_f Density of NC electrons n_n Density of SC electrons n_s

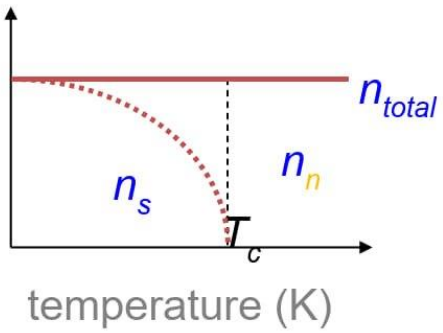

Fig. II.5.A.2: Normal and superconducting electron density in a superconductor vs. temperature (note: $n_{\text{total}} = n_0$).

II.5.A.5 Two-fluid model for superconductors

Basic assumptions of the two-fluid model: all the free electrons of density n_0 of the metal are divided into two groups:

- superconducting electrons of density n_s;
- normal electrons of density n_n.

The total density of the free electrons is $n_0 = n_s + n_n$.

As shown in Fig. II.5.A.2, as the temperature increases from 0 to the critical temperature T_c, the density n_s decreases from n_0 to 0 and the material becomes normal conducting.

$$n_s/n_0 = 1 - (T/T_c)^4 \quad . \tag{II.5.50}$$

II.5.A.6 Complex conductivity

You will probably be only half surprised to read that a superconductor has a value of $R \neq 0$ for fields that are not DC i.e. time-dependent. This can be understood in the framework of the previously mentioned two fluids model, where a population of normal electrons of density n_n and a population of "superconducting electrons" of density $n_s = n_0(1 - T^4/T_c^4)$ coexist such as $n_n + n_s = n_0$ and both give a response to the time-dependent EM fields.

Let's "invent" the complex conductivity σ = of superconducting electrons, starting from II.5.45 and II.5.46 we have

$$\sigma(\omega) = \frac{ne^2\tau}{m_e(1 + j\omega\tau)} \quad , \tag{II.5.51}$$

and taking its limit to $\tau \to \infty$, which means infinite conductivity

$$\lim_{\tau\to\infty} \sigma(\omega) = -j\frac{ne^2}{m_e\omega} \quad , \tag{II.5.52}$$

which gives the conductivity of a perfect conductor. Do you think Eq. II.5.52 looks like a joke: conductivity of a perfect conductor is an imaginary number? There is indeed real physics behind it. Recall the London equations (II.5.A.1), from which we can set up the equivalence Table II.5.A.3.

Table II.5.A.3: Comparison of superconductor (two-fluid model) with normal conductor [51, 52].

Normal metal	Superconductor (London theory)
$\boldsymbol{j} = \sigma_0 \boldsymbol{E} = \frac{n_n e^2 l}{m v_F} \boldsymbol{E}$	$\boldsymbol{j_s} = -\Lambda^{-1} \boldsymbol{A} = \frac{n_s e^2}{m} \boldsymbol{A}$

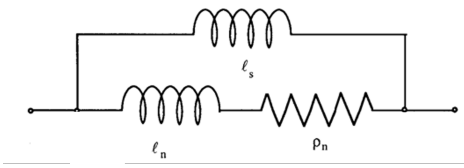

Fig. II.5.A.3: Equivalent circuit for a superconductor.

The value of Λ is the expression of the kinetic inductivity of the "superconducting electrons": basically, the electron pairs have a mass and are accelerated by the RF wave. This is the same as what happens with the magnetic field produced inside an inductor. The conductivity of superconductors becomes the sum of the conductivity of the fraction of normal electrons and that of the fraction of superelectrons

$$\sigma_s = \sigma_1 - j\sigma_2 = \frac{n_0 e^2 \tau}{m} \left(T^4/T_c^4\right) - j \frac{n_0 e^2}{m\omega} \left(1 - T^4/T_c^4\right) \quad , \tag{II.5.53}$$

and

$$\sigma_s = \sigma_1 - j\sigma_2 = \sigma_0 \left(T^4/T_c^4\right) - j \frac{\sigma_0}{\omega\tau} \left(1 - T^4/T_c^4\right) \quad , \tag{II.5.54}$$

where the coefficient of σ_2 is equal to

$$\frac{\sigma_0}{\omega\tau} = \frac{1}{\mu_0 \omega \lambda_L^2} = \frac{1}{\Lambda\omega} \quad , \tag{II.5.55}$$

with $\lambda_L^2 = \frac{\Lambda}{\mu_0}$.

To conclude, one could insert the expression for the complex conductivity $\sigma_s = \sigma_1 - j\sigma_2$ in Eq. II.5.6 and after having some fun with the algebra of complex numbers derive the expressions for the surface resistance R_s and for the surface reactance X_s.

Hint/Caveat: while for a normal conductor the real part and imaginary part of the surface impedance are equal, the situation for a superconductor is completely different; there, the real part can be 1000 times smaller than the imaginary part.

II.5.A.7 Equivalent circuit

If you take the time derivative of $\boldsymbol{j_s} = -\Lambda^{-1}\boldsymbol{A}$ you get the first London equation

$$-\frac{\partial \boldsymbol{A}}{\partial t} = \boldsymbol{E} = \Lambda \frac{\partial \boldsymbol{j}_s}{\partial t} \quad , \tag{II.5.56}$$

where Λ is interpreted as a specific inductance. This justifies representing the complex conductivity of a superconductor with an equivalent circuit of parallel conductors (NC and SC) as seen in Fig II.5.A.3. One can nicely visualise how the resistor is shorted by the lossless inductance at DC (but not for RF).

How can we understand the specific inductance Λ? In analogy to the specific resistance ρ (here: $\sigma = 1/\rho$) it is the inductance of a very small volume element.

II.5.B Main and HOM couplers

RF power has to be fed into a cavity to be transferred to the beam. In a typical superconducting cavity, cavity losses are much smaller than the power transferred to the beam. Being a high-quality resonator with different resonant modes, a small perturbation from the beam can excite resonances away from the fundamental: the power from these high-order modes must be extracted to avoid beam perturbation.

II.5.B.1 Main power couplers, HOM mitigation, and related couplers

Fig. II.5.B.1 shows the LHC solution of the Fundamental (or main) Power Coupler at $400\,\mathrm{MHz}$. You can visualize the rather flat (aspect ratio) of the waveguide (longer side about $0.5\,\mathrm{m}$) feeding the RF power, the ceramic window (and the vacuum flange) in the center of the waveguide, and a long rod ("antenna" on the left-hand side. This long rod is air-cooled at ambient and enters the vacuum of the SC cryogenic cavity.

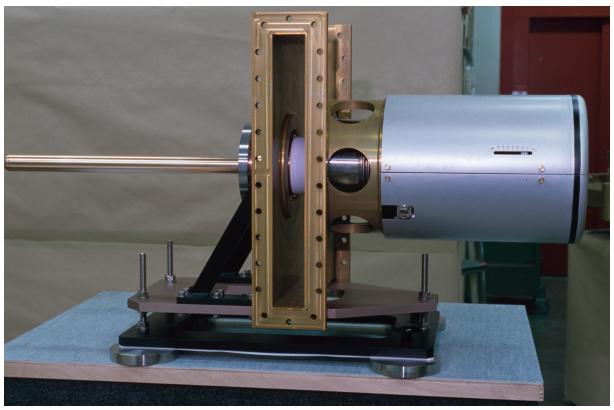

Fig. II.5.B.1: Main power coupler for the LHC $400\,\mathrm{MHz}$ cavity schematic [53].

In Tab II.5.B.1 there is an overview of the CERN power couplers since the 2000's (see also Fig II.5.B.2). It is always good to know what had been done already in order to either copy it (if it worked well) or better not use it when there were problems.

Sometimes a double window coupler is required e.g. when going to cryo and with specific machine requirements (e.g. the European XFEL in DESY). So, in Fig. II.5.B.3 a double window coupler is shown. Unfortunately, with more average power it is difficult to use such a design.

Of course, ceramics have losses. The cold window is difficult to cool down because fully vacuum insulated (on both sides), thus one needs more thermal intercept points, or to increase the sizes. In alternative, to use a coolant, but this increases the vacuum leak risk.

Then comes the question: what is a Higher-Order Modes (HOM) Coupler?

HOM are eigenmodes parasitically excited by a beam in a resonant RF cavity, other than the operating frequency. Each cavity has HOM couplers designed to extract the power and provide a transmission

Table II.5.B.1: Comparison of different types of couplers [54].

Experiment	frequency	power
LHC	400 MHz	500 kW CW SW
SPS 2.0	200 MHz	750 kW CW TW
SPL 2.0	704 MHz	900 kW 10% SW
SPL 3.0	704 MHz	1000 kW 10% SW
Linac4	352 MHz	1000 kW 10% SW
Crab DQW	400 MHz	100 kW CW SW
Crab RFD	400 MHz	100 kW CW SW
ESRF	352 MHz	200 kW CW SW
SOLEIL	352 MHz	200 kW CW SW
APS 1.0	352 MHz	200 kW CW SW
SPS LIU	200 MHz	800 kW CW TW
HG (SPL 3.0)	704 MHz	1500 kW 10% SW
LHC 2.0	400 MHz	500 kW CW SW
APS 2.0	352 MHz	2550 kW CW SW

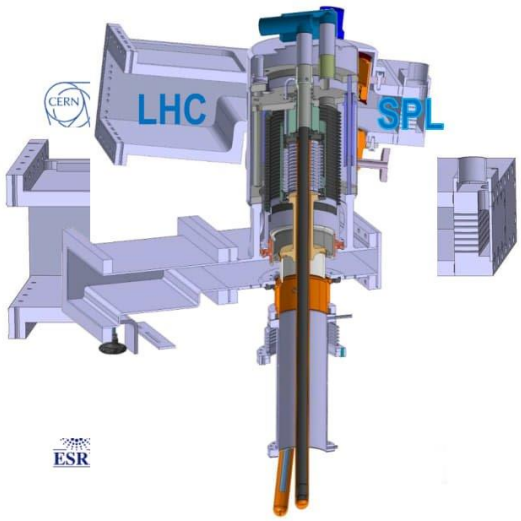

Fig. II.5.B.2: Overview on CERN's power coupler [54].

path at the HOM frequencies and act as a stop-band to the fundamental mode.

Several names exist for the same device: "HOM Couplers", "HOM Filters", "HOM Dampers", and "HOM Suppressors". With future machines (especially true for circular) the HOM couplers will have to extract large amounts of power (several kW) becoming like FPC (Fundamental Power Coupler).

In Fig. II.5.B.4 an LHC HOM coupler(s) is shown. Note that for the big coupler (left) we have a mixture of magnetic and electric coupling, while the small button-type unit on the right is essentially only electric. Furthermore, the external resonant coax lines are not shown here which are essential for the proper functionality of this concept.

Other implementations of HOM couplers from DESY, XFEL are shown in Fig. II.5.B.5.

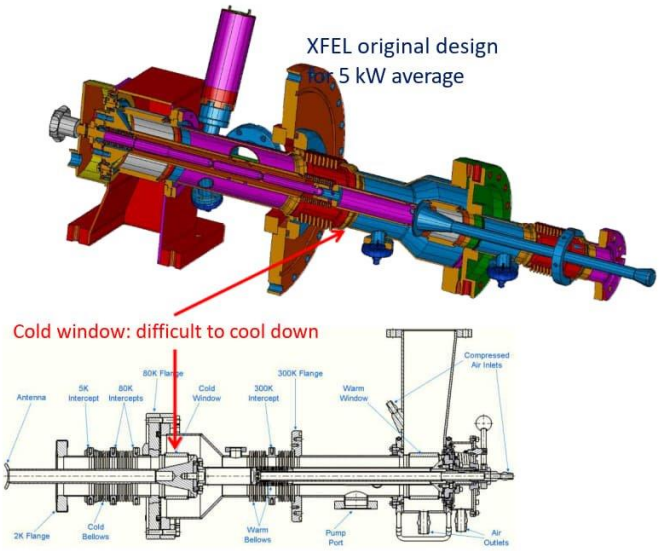

Fig. II.5.B.3: A double windows power coupler [54].

Fig. II.5.B.4: LHC coupling loop for a HOM damper [55].

It is noted that certain HOM couplers require DC bias (kV) to mitigate the multipactor in the coupler region inside the SC cavity.

In Fig. II.5.B.6 an open beam tube is shown which is fine for single-cell cavities, but there is a high cryo-load by thermal radiation.

Finally, ferrites like the one shown in Fig. II.5.B.7 have a low power handling capacity if cold and a higher power handling capacity if warm. However, the mechanical and vacuum design is not easy. The catch is to keep the ferrites away from the field of the fundamental mode.

II.5.B.2 Damping HOMs: Resonant coaxial transmission line dampers

The HOM coupler becomes a resonator coupled to the cavity resonator. It may have two eigenfrequencies because we then have two coupled resonators. The obtainable Q for HOMs is down to 50.

Pros:

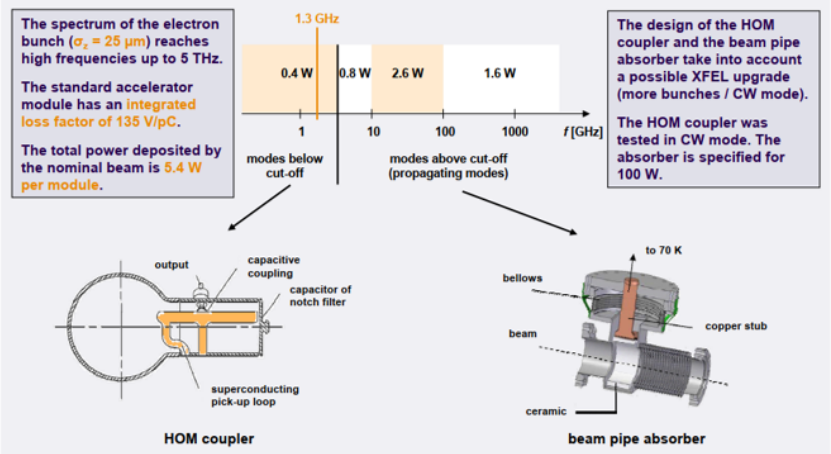

Fig. II.5.B.5: Several implementations of HOM couplers [26].

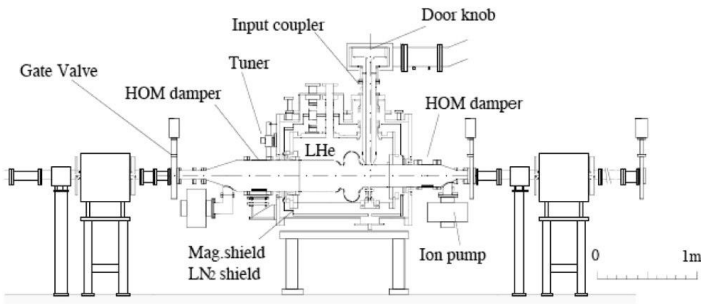

Figure: 1 A sketch of the prototype module in TRISTAN Accumulation Ring.

Fig. II.5.B.6: The Cornell CESR HOM damper concept using ferrite in the beampipe [56].

– Couplers with several resonances possible (HERA, LEP, LHC, ILC are of this type);
– Demountability;
– Fundamental mode rejection:

1. LEP: Fundamental mode E-field rejected by stop-filter in front of HOM coupler,
2. Fundamental mode H-field rejected by loop plane perpendicular to the cavity axis,
3. Risk of detuning the notch filter.

Cons:

– High currents request for superconducting material prepared under ultra-clean conditions (like the cavity) and lHe cooling;
– Prone to electron emission from inside cavity.

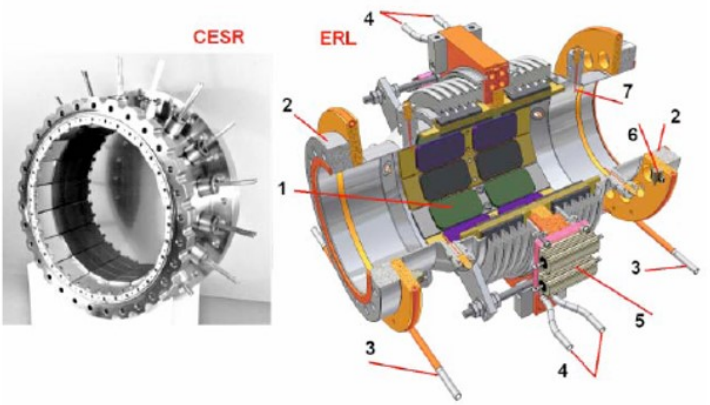

Figure 1: CESR and ERL HOM loads. 1 – absorber plates, 2 – flange to cavity, 3 – 5 K He cooling loop, 4 – 80 K cooling loop, 5 – 80 K heater, 6 – 5 K heaters, 7 – HOM pickup.

Fig. II.5.B.7: The ferrite configuration for the CESR HOM damper [56].

References

[1] Steve Myers, The greatest lepton collider, presentation at Special colloquium for the thirtieth anniversary of the start of operations of LEP, 28 Nov. 2019, Indico CERN.

[2] CERN, LEP radio frequency cavity, exhibition object CERN-OBJ-AC-036, https://cds.cern.ch/record/43993/.

[3] H. Burkhardt, Beam lifetime and beam tails in LEP, Presented at Int. Workshop on Performance Improvement of Electron-Positron Collider Particle Factories, Tsukuba, Japan, 21–24 Sep. 1999, https://cds.cern.ch/record/402586/.

[4] S. Myers, The LEP machine, presentation at LEP Fest, CERN, 11 Oct. 2000, Indico CERN.

[5] E. Chiaveri, Superconducting superconducting cavities: Development/production, presentation at LEP Fest, CERN, 11 Oct. 2000, Indico CERN.

[6] S.M. Anlage, Microwave superconductivity, *IEEE J. Microw.* **1** (2021) 389–402, doi:10.1109/JMW.2020.3033156.

[7] G. Gold, H. Helmreich, Surface impedance concept for modelling conductor roughness, Proc. 2015 IEEE MTT-S Int. Microwave Symp. ,Phoenix, Arizona, USA 17–22 May 2015, pp. 1131–1134, doi:10.1109/MWSYM.2015.7167013.

[8] W. Weingarten, Superconducting cavities: basics, Proc. CERN Accelerator School : Superconductivity in Particle Accelerators, Maui, Hawaii, USA, 3–9 Nov 1994, edited by S. Turner, CERN-96-03 (CERN, Geneva, 1996), pp. 167–189, doi:10.5170/CERN-1996-003.167.

[9] H. Lengeler *et al.*, Superconducting niobium cavities of improved thermal conductivity, *IEEE Trans. Mag.* **21** (1985) 1014–1017, doi:10.1109/TMAG.1985.1063595.

[10] F. Caspers and M. Wendt, JUAS RF course, presentation at CERN Accelerator School, Trondheim, Norway, 18–29 Aug. 2013, Indico CERN.

[11] E. Jensen, RF cavity design, Proc. CERN Accelerator School: Advanced Accelerator Physics Course, Trondheim, Norway, 18–29 Aug. 2013, edited by W. Herr, CERN-2014-009 (CERN, Geneva, 2014), pp. 405–429, doi:10.5170/CERN-2014-009.405.

[12] T. Junginger, Investigations of the surface resistance of superconducting materials, PhD Thesis, Heidelberg U. , 2012, doi:10.11588/heidok.00013728.

[13] F. Caspers *et al.*,Surface resistance measurements and estimate of the beam-induced resistive wall heating of the LHC dipole beam screen, LHC Project Report 307 (CERN, Geneva, 1999), http://cds.cern.ch/record/400683/.

[14] W. Venturini Delsolaro, SC cavity measurements, presentation at EASISchool 3, 29 Sep. 2020, Genoa, Italy, Indico CERN.

[15] C.R.H. McRae *et al.*, Materials loss measurements using superconducting microwave resonators, *Rev. Sci. Instrum.* **91** (2020) 091101, doi:10.1063/5.0017378.

[16] H. Padamsee, Designing superconducting cavities for accelerators, 2004, Proc. CERN Accelerator School on Superconductivity and Cryogenics for Accelerators and Detectors, Erice, Italy, 8–17 May 2002, edited by S. Russenschuck and G. Vandoni, CERN-2004-008 (CERN, Geneva, 2004), pp. 233–252, doi:10.5170/CERN-2004-008.233.

[17] V. Lagomarsino *et al.*, Measurement of niobium superconducting C-band cavities for linear accelerator applications, *IEEE Trans. Mag.* **15** (1979) 25–26, 10.1109/TMAG.1979.1060247.

[18] P. Kneisel, R. Vincon, J. Halbritter, First results on elliptically shaped cavities, *Nucl. Instrum. Meth.* **188** (1981) 669–670, doi:10.1016/0029-554X(81)90280-9.

[19] H. Padamsee, 50 Years of RF superconductivity: A perspective, presentation at The Roots of the LHC Technology: CERN Centennial Superconductivity Symposium, CERN, 8 Dec. 2011, Indico CERN.

[20] R. Boni *et al.*, Design and operation of a multipacting-free 51.4 MHz RF accelerating cavity, *Nucl. Instrum. Meth. A* **274** (1989) 49–55, 10.1016/0168-9002(89)90364-1.

[21] D. Proch, The TESLA cavity: Design considerations and RF properties, Proc. of the Sixth Workshop on RF Superconductivity, CEBAF, Newport News, VA, USA, 4–8 Oct. 1994, edited by R.M Sundelin, pp. 382–397, JACoW.

[22] CERN, Schematic cross section of a 352 MHz superconducting cavity as used in LEP, drawing 1987-05_X_CERN_00042_00032020, May 1987, http://cds.cern.ch/record/2417882.

[23] CERN, Prototype superconducting radio-frequency cavity for LEP, photo CERN-AC-8503636, 14 Mar. 1985, https://cds.cern.ch/record/39285.

[24] CERN, 352 MHz superconducting RF Module, photo 41-08-1993_X_0011_055212019, Aug. 1993, https://cds.cern.ch/record/2580171.

[25] M. Brice, LHC superconducting radio-frequency cavity in the LHC tunnel, photo album CERN-EX-0712013, 20 Dec. 2007, https://cds.cern.ch/record/1077038.

[26] H. Weise, Review of the European XFEL linac system, presentation at XFEL Linac Review Meeting, 26 Mar. 2007, https://www.desy.de/xfel-beam/data/talks/talks/linac_review/weise_-_lin_review_overview_20070326.pdf.

[27] G. Ciovati *et al.* Superconducting prototype cavities for the Spallation Neutron Source (SNS) project, Proc. Part. Accel. Conf. Chicago, IL USA, 18–22 Jun. 2001, edited by P. Lucas and S. Webber, pp. 484-486, doi:10.1109/PAC.2001.987548.

[28] R. Janssens, The ATLAS facility, *Scholarpedia* **5** (2010) 9731, doi:10.4249/scholarpedia.9731.

[29] R. Mehta *et al.*,Design, development and power test of a spiral buncher RF cavity for the high current injector at IUAC, *Nucl. Instrum. Meth. A* **949** (2020) 162776, doi:10.1016/j.nima.2019.162776.

[30] S. Bousson, RF acceleration in linacs (part. 2): Superconducting structures, lecture in the NPAC 2010/11-master programme, https://npac2013.lal.in2p3.fr/2010-2011/Cours/Accelerateurs/NPAC_2010_Accelerator_SB-Lecture6.pdf

[31] JUAS Lecture Archamps, 2008

[32] Gekoppelte Pendel (24 Dec. 2022), in Wikipedia, https://de.wikipedia.org/w/index.php?title=Coupled_pendulum&oldid=229156691.

[33] E. Chiaveri *et al.*, Herbert Lengeler (1931–2021), CERN News, 12 Apr. 2021, https://home.cern/news/obituary/cern/herbert-lengeler-1931-2021.

[34] K. Liao *et al.*, Second sound measurement for SPL cavity diagnostics, Proc. 15th Int. Conf. on RF Superconductivity, Chicago, IL, USA, 25–29 Jul. 2011 (JACoW, Geneva, 2012), pp. 767–772, JACoW.

[35] K. Liao *et al.*, Second sound measurement for SPL cavity diagnostics, poster presented at the Int. Conf. on RF Superconductivity, Chicago, IL, USA, 25–29 Jul. 2011 (JACoW, Geneva, 2012), https://accelconf.web.cern.ch/SRF2011/posters/thpo026_poster.pdf.

[36] O. Brunner, SRF RD program for the Future Circular Collider, 2018, presentation at #3 CERN SRF Workshop, 31 May–1 Jun. 2018, Indico CERN.

[37] C. Antoine, Materials and surface aspects in the development of SRF niobium cavities, EuCARD-BOO-2012-001 (CERN, Geneva, 2012), https://cdsweb.cern.ch/record/1472363.

[38] W. Weingarten, Superconducting cavities, Proc. CERN Accelerator School : RF Engineering for Particle Accelerators, Oxford, UK, 3–10 Apr. 1991, edited by S. Turner, CERN-92-03 (CERN, Geneva, 1992), pp. 318–348, doi:10.5170/CERN-1992-003.318.

[39] S. Posen, Efforts towards first applications of Nb_3Sn SRF cavities, presentation at 20th Int. Conf. on RF superconductivity, Online, 28 Jun. –2 Jul. 2021, Indico Michigan State U.

[40] A. Romanenko *et al.*, Dependence of the residual surface resistance of superconducting radio frequency cavities on the cooling dynamics around T_c, *J. Appl. Phys.* **115** (2014) 184903, doi:10.1063/1.4875655.

[41] S. Pirani, Study of the superconducting medium beta cavity of the European Spallation Source, Ph.D. thesis, Lund U., 2020, https://www.lunduniversity.lu.se/lup/publication/9abfc7ad-adf2-4e03-9a93-176d7671239f.

[42] L.L. Amador *et al.*, Electrodeposition of copper applied to the manufacture of seamless SRF cavities and other accelerator components, accelerator seminar at Thomas Jefferson National Accelerator Facility, 6 Oct. 2021, doi:10.5281/zenodo.10047900.

[43] S. Turner (ed.), Proc. CERN Accelerator School: Superconductivity in Particle Accelerators, Hamburg, Germany, 17–24 May 1995, CERN-96-03 (CERN, Geneva, 1996), doi:10.5170/CERN-1996-003.

[44] G. Muller, Advances in investigations of clean Nb surfaces, presentation at CARE06 Annual Meeting,INFN-LNF, 15–17 Nov. 2006, http://www.lnf.infn.it/conference/care06/TALKS/Mueller.pdf.

[45] CERN, LEP superconducting cavity, photo CERN-AC-9504017, Apr. 1995, CDS.

[46] N. Dhanaraj *et al.*, Fermilab Infrastructure development of single cell testing capability at A0 facility, FERMILAB-TM-2502-TD, TD-09-022 (Fermilab, Batavia, IL, 2009), Inspire.

[47] C. Antoine, How to achieve the best SRF performance: (Practical) limitations and possible solutions, Proc. CERN Accelerator School: Course on Superconductivity for Accelerators, Erice, Italy, 24 Apr. –4 May 2013, edited by R. Bailey, CERN-2014-005 (CERN, Geneva, 2014), pp. 209–245, doi:10.5170/CERN-2014-005.209.

[48] E. Kako *et al.*, Improvement of cavity performance in the Saclay/Cornell/DESY's SC cavities, Proc. Workshop on RF Superconductivity, Santa Fe, NM, USA, 1–5 Nov. 1999, pp. 179–186, JACoW.

[49] S. Posen, M. Liepe, and D.L. Hall, Proof-of-principle demonstration of Nb_3Sn superconducting radiofrequency cavities for high Q0 applications, *Appl. Phys. Lett.* **106** (2015) 082601, doi:10.1063/1.4913247.

[50] E. A. Ilyina *et al.*, Development of sputtered Nb_3Sn films on copper substrates for superconducting radiofrequency applications, *Supercond. Sci. Technol.* **32** (2019) 035002, doi:10.1088/1361-6668/aaf61f.

[51] H. London, F. London, The electromagnetic equations of the supraconductor, *Proc. Roy. Soc. Lond. A,* **149** (1935) 71–88, doi:10.1098/rspa.1935.0048.

[52] A. B. Pippard, W. L. Bragg, An experimental and theoretical study of the relation between magnetic field and current in a superconductor, *Proc. Roy. Soc. Lond. A* **216** (1953) 547–568, doi:10.1098/rspa.1953.0040.

[53] CERN, Main power coupler for the LHC 400 MHz cavity, photo 1998-03-006_X_CERN_04502_0012, Mar. 1998, CDS.

[54] E. Montesinos, High power couplers and HOM couplers, tutorial presented at 20th Int. Conf. on RF Superconductivity, Online, 28 Jun. –2 Jul. 2021, Indico Michigan State U.

[55] R.F. Parodi, Couplers and HOM dampers, Proc. CERN Accelerator School on Superconductivity and Cryogenics for Accelerators and Detectors, Erice, Italy, 8–17 May 2002, edited by S. Russenschuck and G. Vandoni, CERN-2004-008 (CERN, Geneva, 2004) pp. 253–264, doi:10.5170/CERN-2004-008.253.

[56] Cornell University, International Workshop on HOM Damping in Superconducting RF Cavities, 10/2010, https://www.classe.cornell.edu/Events/HOM10/Agenda.html.